

# A VLA Study of Ultracompact and Hypercompact H II Regions from 0.7 to 3.6 cm

M. Sewilo<sup>1</sup>, E. Churchwell<sup>2</sup>, S. Kurtz<sup>3</sup>, W. M. Goss<sup>4</sup>, and P. Hofner<sup>4,5</sup>

## ABSTRACT

We report multi-frequency Very Large Array observations of three massive star formation regions (MSFRs) containing radio continuum components that were identified as broad radio recombination line (RRL) sources and hypercompact (HC) H II region candidates in our previous H92 $\alpha$  and H76 $\alpha$  study: G10.96+0.01 (component W), G28.20–0.04 (N), and G34.26+0.15 (B). An additional HC H II region candidate, G45.07+0.13, known to have broad H66 $\alpha$  and H76 $\alpha$  lines, small size, high electron density and emission measure, was also included. We observed with high spatial resolution (0''.9 to 2''.3) the H53 $\alpha$ , H66 $\alpha$ , H76 $\alpha$ , and H92 $\alpha$  RRLs and the radio continuum at the corresponding wavelengths (0.7 to 3.6 cm). The motivation for these observations was to obtain RRLs over a range of principal quantum states to look for signatures of pressure broadening and macroscopic velocity structure. We find that pressure broadening contributes significantly to the linewidths, but it is not the sole cause of the broad lines. We compare radio continuum and dust emission distributions and find a good correspondence. We also discuss maser emission and multi-wavelength observations reported in the literature for these MSFRs.

*Subject headings:* H II regions — radio lines: ISM — stars: formation

---

<sup>1</sup>The Johns Hopkins University, Department of Physics & Astronomy, 366 Bloomberg Center, 3400 N. Charles Street, Baltimore, MD 21218

<sup>2</sup>University of Wisconsin - Madison, Department of Astronomy, 475 N. Charter St., Madison, WI 53706

<sup>3</sup>Centro de Radioastronomía y Astrofísica, Universidad Nacional Autónoma de México, Apdo. Postal 3-72, 58089, Morelia, Mich. Mexico

<sup>4</sup>National Radio Astronomy Observatory, P.O. Box 0, Socorro, NM 87801

<sup>5</sup>New Mexico Tech, Physics Department, 801 Leroy Place, Socorro, NM 87801

## 1. Introduction

Hypercompact (HC) H II regions represent an earlier evolutionary state than compact and ultracompact (UC) H II regions. These very small ( $\lesssim 0.03$  pc), high electron density ( $n_e \sim 10^{5-6}$  cm $^{-3}$ ) and high emission measure (EM  $\gtrsim 10^8$  pc cm $^{-6}$ ) nebulae are ionized from within by O or B stars and usually are associated with maser emission. Many, but not all, have unusually broad radio recombination lines (RRLs) with full widths at half maximum intensity (FWHM)  $\gtrsim 40$  km s $^{-1}$  (De Pree et al. 1996, 1997; Sewiło et al. 2004a). HC H II regions have rising spectral indices  $\alpha$  (where  $S_\nu \propto \nu^\alpha$ ) from centimeter to millimeter wavelengths with typical values of  $\alpha \sim 1$ , which suggests a range of densities and optical depths in the ionized gas. Broad RRLs (BRRLs) and intermediate sloped ( $-0.1 < \alpha < +2$ ) power-law spectral indices may be associated with the age of HC H II regions, appearing only during a small fraction of the lifetime of the hypercompact phase. There are very dense and compact H II regions, however, that do not have intermediate power-law spectral energy distributions or broad radio recombination lines (e.g., G34.26+0.15 A, Avalos et al. 2006; Sewiło et al. 2004a).

Although possibly related to the age, the physical reason that some HC H II regions do not present BRRLs is poorly understood. The broad linewidths suggest highly dynamic internal structures (e.g., bipolar outflows, expansion, stellar winds, accretion, disk rotation, shocks) as well as electron impact (pressure) broadening. High spatial resolution observations over a wide range of frequencies are required to distinguish the relative contributions from pressure broadening and bulk motion of the gas. Transitions with high principal quantum numbers,  $n$ , are significantly affected by pressure broadening, while low  $n$  transitions are mostly free of pressure broadening and are sensitive to large-scale motions. With high spatial resolution at a range of frequencies, it is possible to distinguish bulk motions from pressure broadening. Observations have shown that both pressure broadening and gas dynamics contribute to line broadening (Sewiło et al. 2008; Keto et al. 2008).

Theoretical progress has been made towards understanding the nature of HC H II regions. The model of hierarchical clumping of the nebular gas proposed by Ignace & Churchwell (2004) was able to reproduce the intermediate values of spectral indices seen in HC H II regions. Tan & McKee (2003) and Keto (2003) proposed models that predict both confinement of the ionized gas in HC H IIs and the BRRL emission. The photoevaporating disk model, originally proposed by Hollenbach et al. (1994) and Lizano et al. (1996) to explain the most compact UC HII regions, has been recognized to be applicable to HC HII regions (Lugo et al. 2004).

Here we report high spatial resolution, multi-frequency Very Large Array<sup>1</sup> (VLA) observations of four candidate HC HII regions with the goal of determining their physical properties. Three sources, G10.96+0.01, G28.20−0.04, and G34.26+0.15, were selected based on an earlier H92 $\alpha$  and H76 $\alpha$  study (Sewiło et al. 2004a). We also observed the HC H II candidate G45.07+0.13 NE, which is known to have broad H66 $\alpha$  and H76 $\alpha$  lines (Garay et al. 1985, 1986), small size, and high electron density (i.e., high emission measure). Additional RRLs were observed to search for systematic broadening with increasing principal quantum number. A strong correlation of line width with principal quantum number would indicate pressure broadening as the main mechanism for line broadening, as opposed to large-scale motions (rotation, outflows, infall, etc.). The rms electron temperature and the rms electron density of the sources can be determined for each transition using the assumption of local thermodynamic equilibrium (LTE). RRLs also provide information on the velocity structure of the sources.

We report detections of the H53 $\alpha$ , H66 $\alpha$ , H76 $\alpha$ , and H92 $\alpha$  RRLs and the 0.7, 1.3, 2.0, and 3.6 cm radio continuum emission with resolutions of 1''.5, 0''.9, 1''.2, and 2''.3, respectively, toward the MSFRs G10.96+0.01, G28.20−0.04, G34.26+0.15, and G45.07+0.13 (hereafter G10.96, G28.20, G34.26, and G45.07). The observations are described in Section 2. In Section 3, we derive physical properties of the nebulae based on continuum observations, and investigate the change of line width with principal quantum number. In Section 4 we investigate the dust emission toward these sources using mid-infrared *Spitzer* Space Telescope GLIMPSE data. We compare the mid-infrared GLIMPSE and radio continuum images with previous maser emission and multiwavelength observations. We discuss the general results in Section 5 and summarize the main conclusions in Section 6.

## 2. The Data

### 2.1. VLA Observations: Continuum and Radio Recombination Lines

The VLA was used to observe H53 $\alpha$ , H66 $\alpha$ , H76 $\alpha$ , and H92 $\alpha$  RRLs toward G10.96, G28.20, G34.26, and G45.07. Table 1 gives the instrumental parameters of the observations. Table 2 summarizes the transitions that we observed toward each source (Sewiło et al. 2004a, and this paper) and the adopted distances.

The first channel of VLA spectral line data (“channel 0”) contains the average of the

---

<sup>1</sup>The National Radio Astronomy Observatory is a facility of the National Science Foundation operated under cooperative agreement by Associated Universities, Inc.

central 75% of the observing bandwidth (generated by vector averaging channels; ?). The broad-band  $uv$  data from "channel 0" were edited and calibrated using the Astronomical Image Processing System (AIPS) software package, and the resulting calibration solutions were applied to the multi-channel spectral-line data. All sources were self-calibrated to increase the dynamic range of the images. The continuum level was determined from a linear fit to the line-free channels. Continuum subtraction was done in the  $uv$  plane with the AIPS task UVLSF. A line-free continuum data set and a 31 channel cube of recombination line emission were constructed. Both data sets were Fourier inverted using weighting intermediate between natural and uniform (Robust=0 in AIPS task IMAGR) and CLEANed in the standard manner. The images were corrected for primary beam attenuation using the AIPS task PBCOR. Integration times and continuum noise values of the final images are listed in Table 3.

Source positions, deconvolved angular diameters, position angles, and total flux densities (Table 3), were determined by elliptical Gaussian fitting using the least-squares AIPS routine JMFIT. Continuum-subtracted line images were used to generate the spatially integrated H $53\alpha$ , H $66\alpha$ , H $76\alpha$ , and H $92\alpha$  line profiles. For each line, the integration was performed approximately over the area enclosed by the 50% contour with respect to the peak value. The subsequent spectral analysis of the RRLs was done using the IDL Programming Language<sup>2</sup>. The spatially integrated line profiles were fitted by a single Gaussian. The results for individual sources are presented graphically in Figs. 1 – 6 for the H $53\alpha$ , H $66\alpha$ , H $76\alpha$ , and H $92\alpha$  RRLs. The continuum images are shown in the same figures; the projected linear scales are based on the kinematic distances listed in Table 2.

## 2.2. Archival Data: VLA and *Spitzer* Space Telescope

In Sewiło et al. (2008), we reported the results of high-resolution ( $0.^{\prime\prime}15$ ) observations of G28.20 N that revealed the shell-like morphology of this HC H $\text{II}$  region. To investigate the morphology of G28.20 N at even higher resolution, here we use VLA K-band A-array archival data (Program ID AZ168) to create the high resolution ( $0.^{\prime\prime}09$ ) continuum image shown in Fig. 4. These observations were taken on 2006 March 14, with a 3.125 MHz bandwidth of 63 channels of 48.828 kHz each. We used line-free channels of these spectral line data to make a self-calibrated continuum image with an rms noise of  $85 \mu\text{Jy beam}^{-1}$ . The measured 1.3 cm flux density of G28.20 N is  $630 \pm 63 \text{ mJy}$ . The synthesized beam is  $0.^{\prime\prime}10 \times 0.^{\prime\prime}08$  at position angle of  $-0^\circ 5$ .

---

<sup>2</sup>[www.ittvis.com/idl](http://www.ittvis.com/idl)

We also present H<sub>2</sub>O, OH, and CH<sub>3</sub>OH maser positions relative to the radio continuum for each HC H II region based on high resolution (interferometric) data from the literature. The relative positional accuracy of 22 GHz H<sub>2</sub>O masers detected toward G45.07 NE is 0."1 (Hofner & Churchwell 1996). The 1665 MHz and 1667 MHz OH masers observed in G10.96 W and G28.20 N have an absolute positional accuracy of  $\sim$ 0."3 in right ascension and  $\sim$ 0."5 in declination (Argon et al. 2000). The absolute positions of the 6.67 GHz CH<sub>3</sub>OH masers in G10.96 W and G28.20 N are accurate to  $\sim$ 1" (Walsh et al. 1998), while the positional uncertainty of the 44 GHz CH<sub>3</sub>OH masers in G45.07 NE is 0."6 (Kurtz et al. 2004). The relative positional accuracy of 22 GHz H<sub>2</sub>O masers detected toward G45.07 NE is 0."1 (Hofner & Churchwell 1996). The distribution of masers is shown in Figs. 1b, 4, and 6 for G10.96 W, G28.20 N, and G45.07 NE, respectively.

We used VLA K-band spectral-line archival data for G28.20 N HC H II region (Program ID AP465) to supplement the single-dish water maser data available for this source in the literature. The observations were taken on 2008 April 4 with the VLA in C configuration. A 3.125 MHz bandwidth with 255 channels of 12.2 kHz each was used. We followed standard VLA data reduction procedures. The synthesized beam is 1."19  $\times$  0."94 at position angle of  $-12^\circ 8$ . The typical rms of a line-free channel is 22 mJy beam<sup>-1</sup>. We determined the positions and peak flux densities of the masers from Gaussian fits to the peak channel of each maser. The H<sub>2</sub>O maser positions and observed parameters are listed in Table 4. The uncertainty of the H<sub>2</sub>O maser positions in G28.20 N is 0."1.

We also investigate dust emission for our sample using data from the *Spitzer* Space Telescope GLIMPSE survey (“Galactic Legacy Infrared Mid-Plane Survey Extraordinaire”, Benjamin et al. 2003; Churchwell et al. 2009). The inner Galactic plane was imaged at 3.6, 4.5, 5.8, and 8.0  $\mu$ m using the IRAC camera (Fazio et al. 2004) on the *Spitzer* Space Telescope. The IRAC spatial resolution ranges from 1."5 to 1."9 between the 3.6 and 8.0  $\mu$ m bands. The IRAC image mosaics were created by the GLIMPSE pipeline. The absolute accuracy of the GLIMPSE point source positions is 0."3 (Meade et al. 2009).

### 3. Results

#### 3.1. Physical Properties of the Sources

Physical properties of the sources were derived from the observed continuum parameters reported in Table 3 using the equations of Mezger & Henderson (1967) and Panagia & Walmsley (1978) for spherical, optically thin, homogeneous, and ionization-bounded H II regions. Panagia & Walmsley (1978) presented modified versions of the Mezger & Henderson

(1967) equations for geometry-dependent physical parameters such as the rms electron density ( $n_{e,rms}$ ), the emission measure (EM), and the mass of ionized gas ( $M_{\text{HII}}$ ). The excitation parameter ( $U$ ) and the Lyman continuum photon flux required to maintain ionization of the nebula ( $N'_c$ ) do not depend on the source size or its morphology and were derived using the formulas from Mezger & Henderson (1967). The continuum optical depth ( $\tau_c$ ) was calculated from the Oster (1961) formula in a form presented by Mezger & Henderson (1967), using EM derived based on the results of Panagia & Walmsley (1978). The derived physical parameters for each source are presented in Table 5. The linear diameter of a sphere listed in Table 5 is the diameter of the spherical model for the source, rather than the apparent Gaussian half-power width of the source reported in Table 3. An optically thin homogeneous sphere has the same peak EM and total flux density as the observed source. The calculations take into account the dependence on the beam size as described in Panagia & Walmsley (1978).

The  $N'_c$  values were used to estimate a lower limit to the spectral type of the exciting star given in the last column of Table 5. The classification is based on the non-LTE, spherically expanding (owing to the stellar wind), line-blanketed (to account for the effects of metals on the atmospheric structure and emerging ionizing flux) model atmospheres derived by Smith et al. (2002) under the assumption that a single star ionizes a dust-free, ionization bounded H II region. The assignment of a given spectral type with  $N'_c$  depends strongly on assignment of effective temperature with spectral type and how accurately stellar atmosphere models reflect reality. For these reasons, spectral types listed in Table 5 are approximations. The stellar spectral type corresponds to the value of radio flux density at the highest frequency observed.

A second set of physical properties of the nebulae was derived based on their peak brightness temperature; these are “peak physical properties” (Wood & Churchwell 1989). These quantities depend only on the peak brightness, not the measured diameter or morphology. Thus, they can be derived for all the sources from our sample including the blended components B and C in the G34.26 complex and the over-resolved component E of G10.96. The brightness temperature  $T_B$  is given by the Rayleigh-Jeans approximation.

The peak optical depth was estimated from  $T_B = T_e(1 - e^{-\tau_c})$  assuming a kinetic temperature of  $T_e = 10^4$  K that is constant over the synthesized beam. The peak emission measure was calculated using the optical depth equation from Mezger & Henderson (1967). The relation  $n_e = \langle n_e^2 \rangle^{1/2} = (EM/\Delta s)^{1/2}$  was used to calculate the rms electron density ( $n_{e,rms}$ ) averaged over the beam. The quantity  $\Delta s$  is the source size along the line of sight through the peak position. We assume the sources in our sample have spherical geometry based on their projected circular symmetry; for  $\Delta s$  we adopt their geometrical mean angular diameters (half-power widths, or “source size” in Table 3) assuming that the extent of the

source along the line of sight is the same as its extent in the plane of the sky. The peak physical properties are given in Table 6.

### 3.2. Radio Recombination Line Analysis

The Gaussian fit parameters of the line profiles are given in Table 7.  $V_{LSR}$  is the central line velocity relative to the local standard of rest,  $FWHM$  is the line full width at half maximum,  $S_L$  is the flux density in excess of the continuum at line center,  $S_C$  is the continuum flux density,  $\frac{S_L}{S_C}$  and  $\int \frac{S_L}{S_C} dv$  are the line-to-continuum ratios at line center and integrated over the line profile, respectively. The continuum flux densities are determined by integrating over the same areas of the source used to generate the line profiles; thus they may be less than the flux densities given in Table 3 (integrated over the entire source). The uncertainties given in Table 7 are the formal  $1\sigma$  (68.3% confidence level) errors of the nonlinear least-squares fit. These uncertainties are lower limits because they do not account for systematic errors.

The measured line widths given in Table 7 are broadened because of the finite velocity resolution of the observations. To determine the intrinsic line widths, the instrumental spectral resolution was deconvolved from the observed lines. The convolution function in the spectral frequency domain was assumed to be a Gaussian function with FWHM of 1.2 times the channel width (or twice the channel width if the spectrum was Hanning-smoothed off-line) and deconvolved from the observed line widths. The deconvolved line widths ( $FWHM_{deconv}$ ) are given in Table 8.

We calculated the LTE electron temperatures  $T_e^*$  for all the sources with reliable RRL measurements using the formula from Rohlfs & Wilson (1986):

$$T_e^* = \left[ \frac{6.985 \times 10^3}{a(\nu, T_e)} \cdot \nu^{1.1} \cdot \frac{(S_L/S_C)_{peak}^{-1}}{FWHM_{deconv}} \cdot \frac{1}{1+Y^+} \right]^{0.87} \quad (1)$$

where  $\nu$  is in GHz,  $FWHM_{deconv}$  is in  $\text{km s}^{-1}$ , and  $T_e^*$  in K.  $Y^+ = N(He^+)/N(H^+)$  is the ratio of ionized He to H atoms and is assumed to be 0.1. The factor  $a(\nu, T_e)$  is approximately 1 (Altenhoff et al. 1960). This equation was derived under several assumptions about H II regions: (1) the structure is plane-parallel, homogeneous and isothermal; (2) all optical depths are small:  $|\tau_l + \tau_c| \ll 1$  and  $\tau_c \ll 1$ ; and (3) the lines can be treated in the LTE approximation.

However, several of the observed sources have relatively high optical depths ( $\tau_C$  from 0.02 to 0.2), causing attenuation of the line-to-continuum ratio. In these cases, the LTE electron temperatures have been calculated using the line-to-continuum ratios corrected for

opacity rather than the measured values:

$$(S_L/S_C)_{corr} = (S_L/S_C)_{peak} \cdot (e^{\tau_c} - 1)/\tau_c. \quad (2)$$

The corrected line-to-continuum ratios and the LTE electron temperatures are listed in Table 8. The uncertainties in  $T_e^*$  were estimated by a linear propagation of errors.

### 3.3. *Spitzer*/IRAC Mid-Infrared Emission

High-spatial resolution mosaics from GLIMPSE (Churchwell et al. 2009) are a unique tool for the study of massive star formation regions. The IRAC 3.6, 5.8, and 8.0  $\mu\text{m}$  bands contain strong polycyclic aromatic hydrocarbon (PAH) features that probe conditions in photodissociation regions (PDRs) that separate the ionized gas in H II regions from the surrounding molecular gas (e.g., Tielens et al. 1993). PAHs are large organic molecules containing  $\gtrsim 50$  C atoms and are very abundant in the ISM (e.g., Sellgren 1984; Allamandola et al. 1989). PAHs are excited by sub-Lyman ultraviolet photons but are destroyed in H II regions by extreme ultraviolet (EUV) radiation (Voit 1992; Povich et al. 2007). Nevertheless, H II regions can be traced by the IRAC 4.5  $\mu\text{m}$  band, which does not contain PAH features. The 4.5  $\mu\text{m}$  emission of H II regions is a combination of thermal emission from small grains, scattered star light, and the Br $\alpha$  recombination line. The 3.6 and 4.5  $\mu\text{m}$  bands are sensitive stellar tracers. The stellar contribution at 5.8 and 8.0  $\mu\text{m}$  is relatively low because the photospheric emission is on the Rayleigh-Jeans tail of the energy distribution and declines rapidly with increasing wavelength.

We present IRAC images in Figs. 7–10. All the images are presented in Galactic coordinates and the intensity is scaled logarithmically. The positions of radio sources are marked or the radio contours are overlaid on the images for reference. Equatorial coordinates are indicated to facilitate comparison with the radio images shown in Figs. 2–6. The GLIMPSE Point Source Catalog (green circles) and Archive<sup>3</sup> sources (red circles) are overlaid on the 3.6  $\mu\text{m}$  images which show the stellar distribution in each field. UC and HC H II regions are usually bright in the IRAC bands; thus they are often saturated in the IRAC images. G28.20 N is saturated in the 8.0 and 4.5  $\mu\text{m}$  bands, G34.26 is saturated in 8.0 and 3.6  $\mu\text{m}$  bands, G45.07 is saturated in all bands. G10.96 and G28.20 S are not saturated in any band. The fact that the sources are saturated does not affect the conclusions we draw in this paper.

---

<sup>3</sup>The GLIMPSE Catalog is more reliable but less complete than the Archive. The GLIMPSE Data Delivery documents are available at <http://irsa.ipac.caltech.edu/data/SPITZER/GLIMPSE/>

The bright IRAC sources suffer from the “electronic bandwidth effect”<sup>4</sup>. This instrumental effect is exhibited only in the 8.0 and 5.8  $\mu\text{m}$  IRAC bands for saturated or bright sources; it produces artifacts appearing as a sequence of sources of decreasing intensity. This effect is seen in the 8.0  $\mu\text{m}$  image of G28.20 N, and 5.8  $\mu\text{m}$  and 8.0  $\mu\text{m}$  images of G34.26 and G45.07 NE. As an example, the source appearing to be blended with G28.20 N slightly to the south in the 8.0  $\mu\text{m}$  image of Figure 8 is not the S component, but rather is an image artifact produced by this effect.

A discussion of the IR emission from individual sources is presented in Section 4.

#### 4. Comments on Individual Sources

In this section, we present the results of our RRL and mid-IR study for the individual sources. We also summarize the previous work on radio, IR, maser, and molecular line (where available) emission from each source.

##### 4.1. G10.96+0.01

The G10.96 MSFR consists of two compact radio continuum components G10.96 E and G10.96 W surrounded by more diffuse ionized gas. They have been detected in radio continuum between 1.4 GHz and 8.6 GHz (Becker et al. 1994; Walsh et al. 1998; Paper I). In Paper I, we reported the detection of a broad H92 $\alpha$  line with a FWHM of  $43.8 \pm 1.5 \text{ km s}^{-1}$  toward the W component. The E component has a linewidth of  $33.6 \pm 2.8 \text{ km s}^{-1}$ , typical for UC H II regions. Based on the 3.6 cm and H92 $\alpha$  observations, we identified G10.96 W as an HC II region candidate (Paper I).

The deconvolved linewidths of the H76 $\alpha$  and H66 $\alpha$  lines from G10.96 W reported in Table 8 are  $28.4 \pm 1.5$  and  $28.0 \pm 0.6 \text{ km s}^{-1}$ , respectively (see Figure 1). These results indicate that the H92 $\alpha$  line is strongly affected by pressure broadening (see the discussion in Section 5.1). For G10.96 E, both H76 $\alpha$  and H66 $\alpha$  lines are narrow with FWHMs of  $19.4 \pm 6.5$  and  $15.0 \pm 4.9 \text{ km s}^{-1}$ , respectively (see Figure 2). These lines are narrower than their H92 $\alpha$  counterpart by over  $10 \text{ km s}^{-1}$ , even if the 30% uncertainty in the FWHMs of the higher frequency lines is accounted for. The difference in FWHMs over a range of RRL transitions in a relatively low density gas indicates that other line broadening mechanisms may be at work in addition to the thermal and turbulent broadening and a small contribution from

---

<sup>4</sup>See <http://ssc.spitzer.caltech.edu/irac/features.html#2C>

pressure broadening (see Section 5.1). Most of the diffuse 3.6 cm radio continuum emission observed near component E (Paper I; HPBW  $\sim 2.^{\circ}3$ ) is resolved out in our 1.3 and 2 cm images (see Figure 2).

Several maser species have been detected toward G10.96. Methanol ( $\text{CH}_3\text{OH}$ ) 6.67 GHz masers were first reported by Schutte et al. (1993) and later confirmed by Walsh et al. (1997), both based on single-dish observations. The high resolution interferometric survey of Walsh et al. (1998) revealed two  $\text{CH}_3\text{OH}$  maser spots in the W component, near the continuum emission peak (see Fig. 1b). Water masers and CS(2-1) emission are reported by Codella et al. (1995) and Bronfman et al. (1996), respectively, based on single-dish observations.

In Figure 7 we present 3.6 and 8.0  $\mu\text{m}$  images of the G10.96 MSFR. These images indicate a close correspondence between the distribution and morphology of dust and ionized gas. The diffuse dust emission from G10.96 E is filamentary, with a size of  $\sim 60'' \times 40''$  ( $\sim 4.1 \times 2.7$  pc at a distance of 14 kpc; Table 2) in RA and Dec, respectively. This filamentary structure is more prominent at 24  $\mu\text{m}$  (MIPSGAL survey; Carey et al. 2009), but is also noticeable at shorter wavelengths. In the 3.6  $\mu\text{m}$  image a possible central ionizing source (high-mass (proto)star) is prominent in the W component. The 3.6, 4.5, 5.8, and 8.0  $\mu\text{m}$  flux densities of the IRAC source (GLIMPSE Archive ID: SSTGLMA G010.9584+00.0219) are  $9.7 \pm 0.9$  mJy,  $58.7 \pm 7.5$  mJy,  $174.2 \pm 12.1$  mJy, and  $395.3 \pm 30.7$  mJy, respectively.

The IRAC images also reveal a cluster of sources around the radio emission peak in component E (see Figure 7). Some of these objects may be ionization sources; however, we can not rule out that some may be background objects. The multiplicity of ionizing (proto)stars may give rise to the multiple-peak morphology of the UC H II region shown in Figure 2. The mid-IR source located near the 3.6 cm peak of G10.96 E in Figure 7 corresponds to one of the two peaks (E2 to the south-west) of the 2 cm emission (Figure 2b). The GLIMPSE Archive provides the 3.6, 4.5, and 5.8  $\mu\text{m}$  flux densities for this source (SSTGLMA G010.9646+00.0098) of  $8.2 \pm 2.7$  mJy,  $13.1 \pm 4.0$  mJy, and  $58.9 \pm 7.6$  mJy, respectively.

#### 4.2. G28.20–0.04

The G28.20–0.04 MSFR hosts two radio continuum components: N and S. Both components were detected in previous radio continuum (0.7 cm – 6 cm, e.g. Kurtz et al. 1994; Walsh et al. 1998; Sewiło et al. 2004a, 2008) and RRL ( $\text{H}92\alpha$  and  $\text{H}53\alpha$ ; Sewiło et al. 2004a, 2008) observations. The N component has been identified as the HC H II region candidate

by Sewiło et al. (2004a) based on the 3.6 cm continuum and H92 $\alpha$  RRL observations. The H92 $\alpha$  lines reported in Paper I have FWHMs of  $74 \pm 3$  and  $35 \pm 1$  km s $^{-1}$  for components N and S, respectively. Higher-frequency RRLs from G28.20 N (H53 $\alpha$ , Sewiło et al. 2008; H30 $\alpha$ , Keto et al. 2008) are significantly narrower than the H92 $\alpha$  line, with line widths of  $39.8 \pm 1.7$  km s $^{-1}$  and  $20.9 \pm 0.6$  km s $^{-1}$ , respectively.

In Fig. 3, we present a 2 cm and a new 7 mm continuum image of G28.20, along with the corresponding H76 $\alpha$  and H53 $\alpha$  line profiles. Both RRLs are narrower than the H92 $\alpha$  line reported in Paper I for both the N and S components. The H76 $\alpha$  and H53 $\alpha$  FWHMs are  $55 \pm 3$  and  $38 \pm 1$  km s $^{-1}$  for component N, and  $24 \pm 4$  km and  $19 \pm 2$  s $^{-1}$  for component S, respectively. The significant increase in line width with increasing quantum number for G28.20 N indicates that pressure broadening is an important (possibly dominant) line broadening mechanism for the H92 $\alpha$  line detected from this source.

Although not evident in Figure 3, we detect marginal evidence for 7 mm continuum emission at the south-east border of G28.20 N. The emission is slightly more evident in the 6 cm CORNISH image (C. Purcell, personal communication). We do not report parameters for this marginal detection, but note the possible presence of a non-thermal source at this position. In addition, our continuum images — at both 7 mm and 2 cm — show evidence for a new source, with a rising spectral index, just to the east of G28.20 S. We refer to this source as G28.20 S1 (see Figure 3a), and report approximate values for its parameters in Table 3.

However, Sewiło et al. (2008) showed that gas dynamics also contributes to line broadening in G28.20 N. The morphology and velocity structure of G28.20 N was resolved in their high resolution ( $\sim 0''.15$ ) 7 mm continuum and H53 $\alpha$  VLA observations. The source appears as a shell-like structure with an inner radius of 1100 AU and an outer radius of 2500 AU. They detected a velocity gradient of  $10^3$  km s $^{-1}$  pc $^{-1}$  along the minor axis of the continuum source, from which they inferred a rotating torus around an  $\sim 30$  M $_{\odot}$  central object. Based on line broadening and splitting along the major axis, they also suggested the presence of an outflow.

#### 4.2.1. Molecular Gas Kinematics

G28.20 N has also been the target of high resolution molecular line observations by Qin et al. (2008), who proposed the existence of a hot core in G28.20 N. They used the SMA to image transitions in CH<sub>3</sub>CN, CO, <sup>13</sup>CO, SO<sub>2</sub>, OCS, and CH<sub>3</sub>OH with 1'' resolution. These authors derived a CH<sub>3</sub>CN rotation temperature of  $308 \pm 22$  K, inferred an H<sub>2</sub> density

$>10^7 \text{ cm}^{-3}$ , and an age of G28.20 N of  $1.5 \times 10^4$  years. These properties, together with the small size ( $<0.04 \text{ pc}$ ) fulfill the standard hot core criteria (size  $\lesssim 0.1 \text{ pc}$ , density  $\gtrsim 10^7 \text{ cm}^{-3}$ , and temperature  $\gtrsim 100 \text{ K}$ ; Kurtz et al. 2000). Spectra of SO<sub>2</sub>, OCS, and CH<sub>3</sub>OH have similar radial velocities and line widths as CH<sub>3</sub>CN; thus they likely originate in the hot molecular core. Qin et al. (2008) argue that <sup>13</sup>CO emission originates outside of the hot molecular core, since the excitation temperature and H<sub>2</sub> density are lower than those derived from the CH<sub>3</sub>CN line. The <sup>13</sup>CO spectrum shows blueshifted absorption and redshifted emission with the absorption and emission peaks aligned with the source rotational axis (i.e., the SE-NW direction; Sewiło et al. 2008). Based on the <sup>13</sup>CO distribution and line profile, Qin et al. (2008) concluded that <sup>13</sup>CO traces an outflow from the molecular core over a linear scale of  $\sim 0.1 \text{ pc}$ .

The OCS position-velocity diagram for the NE-SW direction across the continuum source G28.20 N shows two velocity peaks (95 and 97 km s<sup>-1</sup>) separated by 0''.2. This velocity difference corresponds to a NE-SW velocity gradient of  $\sim 400 \text{ km s}^{-1} \text{ pc}^{-1}$  (Qin et al. 2008). A similar velocity pattern was observed in the K=5 component of the CH<sub>3</sub>CN (J=12-11) transition detected toward G28.20 N (S.-L. Qin, private communication). The infall and outflow were previously reported by Sollins et al. (2005), based on VLA observations of ammonia (HPBW from  $\sim 0''.3$  to  $\sim 3''$ ).

Based on the same SMA data previously used by Qin et al. (2008), Klaassen et al. (2009) reported a detection of the SO<sub>2</sub> and OCS velocity gradient of  $\sim 150 \text{ km s}^{-1} \text{ pc}^{-1}$  in a roughly N-S direction (as opposed to the NE-SW direction suggested by Qin et al. 2008). Klaassen et al. (2009) also suggested the presence of a CO outflow in the NE-SW direction. Qin et al. (2008) found that the CO data are inconclusive due to the contamination from the infall; as mentioned above, they suggested an outflow in the SE-NW direction based on the <sup>13</sup>CO data. The detection of the H53 $\alpha$  velocity gradient in the NE-SW direction by Sewiło et al. (2008) supports the Qin et al. (2008) interpretation.

#### 4.2.2. Maser Emission

Numerous masers have been detected toward the G28.20 MSFR: 1665 and 1667 MHz OH (Argon et al. 2000), 22 GHz H<sub>2</sub>O (Han et al. 1998; Kurtz & Hofner 2005; this paper), and 6.67 GHz CH<sub>3</sub>OH (Walsh et al. 1998). G28.20 was also observed with arcminute resolution in the excited OH transitions at 6035 MHz (Caswell & Vaile 1995b; Caswell 2003) and 6030 MHz (Caswell 2003). The OH, H<sub>2</sub>O, and CH<sub>3</sub>OH maser emission is associated with component N (see Fig. 4).

#### 4.2.3. Dust Emission

Spitzer IRAC images of G28.20 at 8.0 and 3.6  $\mu\text{m}$  are shown in Fig. 8. The 8.0  $\mu\text{m}$  image shows that G28.20 is located toward an elongated region of high extinction (infrared dark cloud, IRDC) stretching over at least 2' ( $\sim 3.3$  pc at 5.7 kpc) in a roughly NE-SW direction. This IRDC is probably the natal molecular cloud from which the protostars in G28.20 are forming. Figure 8b shows the 3.6  $\mu\text{m}$  image of G28.20 MSFR. The contours of the 2 cm radio emission indicate the position of the N and S components. The mid-IR sources from the GLIMPSE Catalog/Archive are indicated by circles. A bright source, detected in K<sub>s</sub>-band and all four IRAC bands, coincides with G28.20 N. A much weaker source, detected at 3.6 and 4.5  $\mu\text{m}$ , coincides with G28.20 S. Midway between the two radio components, a third IR source is a near-IR (JHK<sub>s</sub>) source (also detected at 3.6  $\mu\text{m}$ ). This source does not have a radio counterpart and may be a foreground object or a less deeply embedded object.

Both G28.20 N and G28.20 S have counterparts in the GLIMPSE Archive: SSTGLMA G028.2003-00.0493 and SSTGLMAG028.1984-00.0501, respectively. The mid-IR source corresponding to G28.20 N is significantly brighter than the sources that matches G28.20 S. The 3.6 and 4.5  $\mu\text{m}$  flux densities are  $358.4 \pm 18.9$  mJy and  $2123.0 \pm 99.3$  mJy for component N, and  $2.1 \pm 0.3$  mJy and  $8.9 \pm 1.2$  mJy for component S. The 5.8  $\mu\text{m}$  flux density of G28.20 N is  $3892.0 \pm 98.6$  mJy.

### 4.3. G34.26+0.15

Four radio continuum components (A–D) and two infrared sources (E and F, Campbell et al. 2000) have been identified in the G34.26 MSFR. Component C is a prototypical cometary UC H II region with a compact head toward the east and a diffuse tail to the west (e.g., Reid & Ho 1985; Garay et al. 1986; Sewiło et al. 2004a). Components A and B, located to the east of component C, are HC H II region candidates. A more evolved component (D), located south-east of components A–C, is thought to be an H II shell with a diameter  $\sim 1'$ , expanding within an ambient density gradient (Fey et al. 1994).

We detected H53 $\alpha$  emission toward G34.26 components A, B, and C. The line parameters are presented in Tables 7 and 8; line profiles and the 7 mm continuum image are shown in Figure 5.

The H76 $\alpha$  (Paper I) and H53 $\alpha$  (this paper) lines from G34.26 A are narrow, with FWHMs of  $\sim 22$  km s $^{-1}$ , consistent with a combination of thermal and turbulent broadening. The H53 $\alpha$  linewidth of component C is  $50.2 \pm 6.4$  km s $^{-1}$ , in good agreement with the H76 $\alpha$  linewidth of  $55.5 \pm 1.9$  km s $^{-1}$  reported by Garay et al. (1986). These authors demonstrate

that this relatively broad linewidth probably results from microturbulent motions having a velocity of  $\sim 30 \text{ km s}^{-1}$ . Component B has a broad H $76\alpha$  line of FWHM  $48.4 \pm 4.4 \text{ km s}^{-1}$  (Paper I); however the H $53\alpha$  line is  $\sim 15 \text{ km s}^{-1}$  narrower (see Table 8) indicating that the H $76\alpha$  line has a substantial contribution from pressure broadening. Also notable is the higher H $53\alpha$  line center velocity for component B; the velocity is more than  $15 \text{ km s}^{-1}$  higher than for either component A or C. It is unclear if this velocity difference is important to understand the nature of component B. Hatchell et al. (2001) considered component B as a strong candidate for the driving source of the SiO outflow; if this is the case, there may be a dynamic explanation for the higher H $53\alpha$  velocity.

If we assume no contribution to the component A and B line widths from large scale motions and a non-thermal (turbulent) contribution of  $5 \text{ km s}^{-1}$  (FWHM; Cesaroni et al. 1991, Plume et al. 1997, Sewiło et al. 2008), then we can determine an upper limit for pressure broadening from the H $76\alpha$  line. The electron temperatures for the A and B components are 5700 K and 5300 K, respectively (Paper I). Thus, the thermal plus turbulent contribution to the line width is  $\sim 17$  and  $\sim 16 \text{ km s}^{-1}$  for components A and B, respectively. The resulting upper limits for the pressure broadening contribution to the H $76\alpha$  linewidth (calculated as described in Sewiło et al. 2008) are  $\sim 10 \text{ km s}^{-1}$  and  $\sim 43 \text{ km s}^{-1}$  for the A and B components, respectively.

Components A and B meet the criteria for HC H II regions (Paper I; Avalos et al. 2006; this paper). The diameters, electron densities and emission measures derived in Paper I based on high-resolution ( $\sim 0.^{\prime\prime}5$ ) 2 cm observations are 0.008 pc and 0.006 pc (assuming a distance of 3.7 kpc);  $1.4 \times 10^5 \text{ cm}^{-3}$  and  $2.2 \times 10^5 \text{ cm}^{-3}$ ;  $2.2 \times 10^8 \text{ pc cm}^{-6}$  and  $4.3 \times 10^8 \text{ pc cm}^{-6}$ , respectively. However, both components A and B have a relatively low turnover frequency of  $\sim 10 \text{ GHz}$  (Avalos et al. 2006). The physical parameters derived in this paper (see Table 5) for component A agree with the Paper I results. No physical parameters for component B can be derived because this source is partially blended with component C at the resolution of  $1.^{\prime\prime}5$ .

Avalos et al. (2009) resolved G34.26 A and B with  $0.^{\prime\prime}05$  resolution VLA observations and detected possible limb brightening in both sources. They used spherical shell models with power-law density gradients ( $n_e \propto r^{-\alpha}$ ) to explain their observations. They showed that the 7 mm intensity profiles, radio continuum spectra, and angular sizes of both G34.26 A and B can be reproduced by a shell of inner and outer radii  $\sim 400 \text{ AU}$  and  $\sim 1000 \text{ AU}$ , respectively, and a density gradient  $\alpha \sim 0.3\text{--}1.0$ . This physical picture is quite similar to what has been proposed for G24.78+0.08 A1 (Beltrán et al. 2007) and G28.20-0.04 N (Sewiło et al. 2008).

#### 4.3.1. Maser Emission

Maser emission is detected in G34.26 including H<sub>2</sub>O (Hofner & Churchwell 1996), OH at 1665 and 1667 MHz (Garay et al. 1985; Gaume & Mutel 1987, Gasiprong et al. 2002), OH at 6 GHz (Caswell & Vaile 1995b), and CH<sub>3</sub>OH at 6.67 GHz (Menten 1991) and 44 GHz (Kurtz et al. 2004). The H<sub>2</sub>O maser spots are distributed ahead of and projected onto the cometary arc of component C, while most of the OH masers are more tightly confined to a parabolic arc along the eastern edge of component C (e.g., Gasiprong et al. 2002). A cluster of OH 1665 MHz masers is associated with component B. No OH, H<sub>2</sub>O, or CH<sub>3</sub>OH maser emission is detected toward component A. Several of the authors cited above provide detailed discussions of the relation between the masers and other physical phenomena within the MSFR.

High angular resolution molecular line observations (Keto et al. 1992; Garay & Rodríguez 1990; Heaton et al. 1989; Hofner & Churchwell 1996; Mookerjea et al. 2007) indicate that the molecular gas lies roughly between components A, B, and C (hot core). In particular, there is no evidence for localized molecular peaks coincident with components A or B.

#### 4.3.2. Dust Emission

Mid-IR emission from components A, C, and D of G34.26 was detected at wavelengths from 8 to 20.6  $\mu\text{m}$  with resolutions  $< 2''$  by Keto et al. (1992) and Campbell et al. (2000). Their observations failed to detect component B, suggesting that this source is more deeply embedded. They also showed that component C does not have a cometary morphology in the mid-IR; the general discrepancy between mid-IR and radio morphologies is discussed by Hoare et al. (2007). Campbell et al. (2000) detected two additional sources, which they designated E and F. Component F is located about 17'' south of component C in the 20.6  $\mu\text{m}$  image; component E is located 2'' south of and is blended with component C (Campbell et al. 2000). Mid-IR sources C and E coincide with the arc of the cometary H II region (see Fig. 9) and were resolved into four individual sources in the sub-arcsecond resolution 10.5  $\mu\text{m}$  and 18.1  $\mu\text{m}$  images of De Buizer et al. (2003).

The IRAC images of G34.26 illustrate how active and dynamic this MSFR is. Fig. 9 shows the 4.5  $\mu\text{m}$  and 3.6  $\mu\text{m}$  images. The 8.0 and 5.8  $\mu\text{m}$  emission is similar to that shown in Fig. 9 except that the outflow is only detected at 4.5  $\mu\text{m}$  (see below). The IR counterparts of radio components A and C cannot be distinguished from one another, owing to very bright, diffuse emission in the IRAC bands. Also, IR components E and C are blended. IR component F was detected in all bands. The large ring of emission south-east of components

A-C (see left panel of Fig. 9) corresponds to the D radio component of the G34.26 complex. Comparison of the 2 cm image of Fey et al. (1994) with the IRAC images shows that this IR ring has roughly the same angular extent ( $\sim 1'$  radius) and brightness distribution (75% complete ring of emission with an opening to the NE) as at radio wavelengths.

The IRAC images reveal multiple IR sources that were not detected by earlier infrared observations. Nevertheless, component B remains undetected, even in the IRAC images. The point sources listed in the GLIMPSE Catalog and Archive are shown in Fig. 9. The high-resolution 2 cm radio contours (Paper I) are overlaid on the  $3.6\ \mu\text{m}$  image to indicate the positions of the A-C radio components; IR sources E and F are also marked. Only G34.26 C has a counterpart in the GLIMPSE Archive (SSTGLMA G034.2572+00.1533) with flux densities of  $4857 \pm 278$  mJy and  $4481 \pm 155$  mJy at 4.5 and  $5.8\ \mu\text{m}$ , respectively.

One of the most prominent features in the color composite image of G34.26 (Fig. 9) is an outflow detected as an Extended Green Object (EGO, Cyganowski et al. 2009). Molecular outflows are particularly strong in the IRAC  $4.5\ \mu\text{m}$  band because of shocked H<sub>2</sub> and/or CO line emission (Cyganowski et al. 2008). The source of the outflow is unknown. Moreover, other outflows appear in SiO (Hatchell et al. 2001) and  $^{13}\text{CO}$  (Matthews et al. 1987). The latter two outflows are not well-aligned with the EGO, suggesting that they are different outflows arising from different driving sources.

#### 4.4. G45.07+0.13

G45.07 consists of a bright NE component ( $S_{2\text{cm}} = 620$  mJy) and a much fainter SW component ( $S_{2\text{cm}} = 40$  mJy), separated by  $\sim 6''$  (see Fig. 6). The SW component was first detected by Garay et al. (1986) at 2 cm and designated G45.07 A. Both NE and SW components are unresolved in our radio continuum maps. High resolution (HPBW  $\sim 0''.1$ ) observations by Turner & Matthews (1984) of the NE component revealed a clumpy ring with a gap to the west which they interpreted as a shell with an inner cavity produced by a stellar wind from a hot central star. However, Garay et al. (1986) suggested that the ring-like structure may be the ionized inner wall of an accretion disk. They further suggest that the ring is expanding at  $\sim 10\ \text{km s}^{-1}$  (owing to a hot stellar wind) and is inclined by  $\sim 75^\circ$  to the line of sight. The H $76\alpha$  RRL integrated over the whole NE component is broad with a FWHM of  $48.1 \pm 0.9\ \text{km s}^{-1}$  (Garay et al. 1986). Garay et al. (1985) also detected broad H $66\alpha$  emission with a FWHM of  $42.3 \pm 2.3\ \text{km s}^{-1}$ . Keto et al. (2008) reported a detection of the H $30\alpha$  line toward the NE component with FWHM of  $33.2 \pm 4.2\ \text{km s}^{-1}$ .

We detected H $92\alpha$  emission toward both the NE and SW components of G45.07; how-

ever, we were not able to determine reliable line parameters and physical properties of the sources based on these data. The H92 $\alpha$  line observed toward the SW component is very narrow relative to the channel width ( $16.9 \text{ km s}^{-1}$ ) preventing a reliable Gaussian analysis. We estimate that the peak line-to-continuum ratio of this line is  $\gtrsim 0.07$ . For the NE component, the H92 $\alpha$  line has a very poor signal-to-noise ratio, likely the result of the high optical depth which attenuates the line. The peak line-to-continuum ratio for this line is  $\sim 0.03$  and the deconvolved FWHM of  $40 \pm 9 \text{ km s}^{-1}$ .

Hunter et al. (1997) reported a molecular outflow centered on G45.07 NE based on observations at millimeter and submillimeter wavelengths and in the CO(6-5) and CS(2-1) molecular lines. Infall was also detected by redshifted CS(2-1) absorption, confirming the young age of this source. The outflow axis is aligned spatially and kinematically with the H<sub>2</sub>O maser spots in G45.07 NE (Hofner & Churchwell 1996), suggesting that the masers form in warm and dense shocked gas at the inner edges of the outflow lobes (Hunter et al. 1997).

Several masers have been detected in the NE component of G45.07, while no maser emission is associated with the SW component (see Fig. 6b). Hofner & Churchwell (1996) detected four clusters of water masers in the area, three of which are closely associated with the cm continuum emission from the NE component. The fourth group is located about  $2''$  North of the NE component and is not coincident (in high resolution images) with any radio continuum emission. The H<sub>2</sub>O masers are intermixed with 1665 and 1667 MHz OH masers at these two locations (Garay et al. 1985; Argon et al. 2000). A 44 GHz CH<sub>3</sub>OH maser was detected  $\sim 6''$  north of the NE component by Kurtz et al. (2004). Single-dish observations by Menten (1991) and Caswell et al. (1995a) revealed methanol 6.67 GHz masers.

#### 4.4.1. Mid-Infrared Emission

High-resolution observations (from  $1.''1$  to  $1.''7$ ; De Buizer et al. 2003, 2005; Kraemer et al. 2003) at mid-IR wavelengths from  $10.5 \mu\text{m}$  to  $20.6 \mu\text{m}$ , revealed three mid-IR components associated with the G45.07 MSFR, designated KJK 1, 2, and 3 by Kraemer et al. (2003). The brightest component, KJK 1, is coincident with G45.07 NE and contributes roughly half of the total (KJK 1-3) flux at  $12.5 \mu\text{m}$  and  $20.6 \mu\text{m}$  (Kraemer et al. 2003). The second brightest component, KJK 2, lies  $2''$  north of KJK 1, coincident with the water maser group  $2''$  north of the NE component (Hofner & Churchwell 1996, see discussion above); this source is a good candidate for a hot molecular core (HMC). Based on the mid-IR luminosities, De Buizer et al. (2003) estimated that the putative HMC in G45.07 would contain an O-type star if it is heated by a single star. KJK 2 may drive the outflow reported by Hunter et al.

(1997). The third mid-IR component, KJK 3, corresponds to the SW component of G45.07.

GLIMPSE 3.6 and 4.5  $\mu\text{m}$  IRAC images of the G45.07 MSFR are presented in Fig. 10. At IRAC bands, G45.07 is a bright source. The KJK 1 and 2 sources are not well-resolved in these images but are clearly apparent in Fig. 10. KJK 3 is very faint at shorter IRAC bands, but is bright at 8  $\mu\text{m}$  where PAH emission dominates.

The GLIMPSE Catalog and Archive sources shown in Fig. 10 reveal the positions of (proto)stars that may be responsible for exciting PAH emission. In general there is a good correspondence between the distribution of dust and gas in G45.07; however the dust emission extends beyond the region of ionized gas emission at 3.6 cm because the PAH contribution to this band traces the PDR that surrounds the nebula. The correspondence in projected emission does not necessarily imply that ionized gas and dust are well mixed. Additionally, the VLA filters out extended emission and much of the extended IR emission is instrumental (sidelobes of the *Spitzer* point spread function), making the interpretation of the data more difficult.

## 5. Discussion

### 5.1. Radio Recombination Lines

We detected RRLs from all four sources in our sample (see Table 2 for details on the observed transitions). Figure 11 shows the relation between the widths (FWHMs) of the RRLs and frequency for these sources. Regions classified as HC H II candidates and UC H II regions are plotted separately in Figure 11a and 11b, respectively. The dashed vertical lines indicate the rest frequencies of the observed transitions.

The change of observed Gaussian line widths with frequency (or principal quantum number) presented in Figure 11 clearly illustrates the effects of pressure broadening based on our data. The limited sensitivity that is typical of very high spatial resolution RRL observations rarely permits the Voigt profile to be seen (Roelfsema & Goss 1992). Very broad bandwidths and good signal-to-noise ratios in the weak RRL wings are a prerequisite to fit Voigt profiles; our data are not adequate for such a fitting procedure.

Figure 11a shows that the lines from HC H II regions (except G34.26 A), particularly the lower-frequency transitions, are too broad to be the result of a combination of thermal and turbulent broadening only. If an electron temperature of 10,000 K and turbulent velocity of 5 km s $^{-1}$  are assumed, the contribution from thermal and turbulent motions to the line widths would be only  $\sim$ 22 km s $^{-1}$ . The change in line width with transition apparent in

Figure 11a strongly suggests that pressure broadening is a dominant broadening mechanism. Owing to the rapid change of pressure broadening with principal quantum number  $n$  (FWHM of pressure broadening  $\propto n^{7.4}$ ; Brocklehurst & Seaton 1972), the lower-frequency lines are affected much more strongly by pressure broadening than the higher-frequency lines. At high frequencies, pressure broadening becomes negligible, thus line widths should be dominated by thermal, turbulent, and bulk motions. Even though pressure broadening depends so strongly on  $n$ , accurate adherence to the  $n^{7.4}$  dependence is not expected because of other dependences on electron density and electron temperature, which vary within H II regions (e.g. Roelfsema & Goss 1992).

Pressure broadening is less strongly dependent on electron density than on the principal quantum number (FWHM  $\propto n_{e,true}$ , where  $n_{e,true}$  is the local true electron density; Brocklehurst & Seaton 1972). The true electron density traced by line widths is higher than the rms electron density measured from the continuum data. The difference depends on the filling factor  $f$  of the H II region ( $f = n_{e,rms}^2/n_{e,true}^2$ ). The filling factor is the fraction of the total volume that is occupied by dense gas; thus it is a measure of clumpiness in the H II region. The higher electron density results in more pressure broadening, thus this effect may explain the observed increase in line width for the relatively low rms electron density UC H II regions G10.96 E and G28.20 S (see Figure 11b).

Sources G28.20 N, G28.20 S, G34.26 B and G34.26 C have been observed in high frequency RRLs: H30 $\alpha$  for G28.20 N and H53 $\alpha$  for the remaining three sources. By comparing these high frequency lines with lower frequency (and hence pressure-broadened) lines, we can determine  $n_{e,true}$ . Comparing these densities with the *rms* values from the continuum observations then provides an estimate of the filling factor. Sources showing the steepest slopes in the FWHM versus frequency plot of Figure 11 will have  $n_{e,true}$  much greater than  $n_{e,rms}$ , and hence have the smallest filling factors.

The largest change of linewidth with frequency of the RRL is obtained for G28.20 N. Sewilo et al. (2008) obtained an  $n_{e,true}$  more than an order of magnitude higher than  $n_{e,rms}$  and a filling factor of  $6 \times 10^{-4}$  for this source. G28.20 S, on the other hand, shows only a  $4 \text{ km s}^{-1}$  change in linewidth between the H76 $\alpha$  and H53 $\alpha$  lines. We determine an  $n_{e,true}$  of  $(1.2 \pm 0.7) \times 10^5 \text{ cm}^{-3}$  compared to the continuum value of  $n_{e,rms} = 8 \times 10^3 \text{ cm}^{-3}$ , thus yielding a filling factor of  $5 \times 10^{-3}$ .

For G34.26 components B and C we calculate true electron densities of  $(4.2 \pm 0.9) \times 10^5 \text{ cm}^{-3}$  and  $(4 \pm 2) \times 10^5 \text{ cm}^{-3}$ , respectively, resulting in filling factors of 0.3 and 0.06.

We note that the true electron densities and hence the filling factors are calculated under the assumption that the H53 $\alpha$  linewidth has *no* contribution from pressure broadening. If

this assumption is not true, then the values we report should be considered as limits; the true electron densities will be higher and the true filling factors will be smaller.

The broad linewidths ( $\text{FWHM} \geq 40 \text{ km s}^{-1}$ ) detected toward the HC HII candidates (Figure 11a) probably have a contribution from bulk motions: G28.28 N has been related to rotation and possible outflow; G34.26 B to an outflow; and G45.07 NE to expansion (see Section 4.4). All these phenomena may contribute to line broadening. For the UC HII region G34.26 C (Figure 11b), Garay et al. (1986) proposed that the relatively broad H $76\alpha$  line results from microturbulent motions of  $\sim 30 \text{ km s}^{-1}$  (see Section 4.3).

## 5.2. Continuum Emission

The continuum observations of MSFRs G10.96 and G28.20 at two wavelengths (Table 3) allow a determination of the spectral index for the individual sources in these regions, provided that the reliable flux density measurements can be made (G10.96 W, G28.20 N). For consistency, the two continuum images for each region (1.3 cm and 2 cm for G10.96; 7 mm and 2 cm for G28.20) were convolved to a common resolution before measuring the flux densities. For G10.96 W, the 1.3 cm and 2 cm flux densities of  $296 \pm 15 \text{ mJy}$  and  $288 \pm 15 \text{ mJy}$ , respectively, give a spectral index of  $+(0.07 \pm 0.17)$ , indicating that this source is in the optically thin regime. The 7 mm and 2 cm flux densities of G28.20 N are  $723 \pm 37 \text{ mJy}$  and  $490 \pm 25 \text{ mJy}$ , respectively, indicating a spectral index of  $+(0.4 \pm 0.1)$ . This value suggests that the HII region has a turnover wavelength in the 2 cm – 7 mm range. The flux density distribution for G28.20 N, based on high-resolution interferometric observations covering the wavelength range from 6 cm to 1.3 mm, is shown in Fig. 12. The plot shows the spectrum becoming optically thin in the 20 – 50 GHz range.

We found that G28.20 N is very similar to the well-studied HC HII region G24.78+0.08 A1 (Beltrán et al. 2007) in terms of physical properties, kinematics (rotation, infall, outflow), morphology (shell-like), and association with masers. The flux density distributions of these sources are similar in terms of the shape and the turn-over frequency (Beltrán et al. 2007; Fig. 12). Neither of these HC HII regions has a rising spectrum to millimeter wavelengths (as do G9.62+0.19 E and G75.78+0.34 ( $\text{H}_2\text{O}$ ), see Franco et al. 2000). The shell-like morphology appears to be a common feature of the HC HII regions. Besides G28.20 N and G24.78+0.08 A1, the A and B components in G34.26, and also G45.07 NE, show a shell morphology in high resolution images reported by Avalos et al. (2009) and Turner & Matthews (1984), respectively.

### 5.3. Distribution of Masers

We investigated the distribution of maser emission in MSFRs from our sample. We found that maser emission is only detected toward sources with broad RRLs (typically the most compact and dense sources in the UC/HC H II region complexes): G10.96 W, G28.20 N, G34.26 B and C, and G45.07 NE.

In Figure 4 we show the maser positions for G28.20 N overlaid on the continuum and thermal molecular line emission. The OH masers are distributed linearly over a region  $\sim 1.^{\prime\prime}4$  (or  $\sim 0.04$  pc; Figure 4a) with a velocity gradient of  $\sim 150$  km s $^{-1}$  pc $^{-1}$ . The velocities increase from  $\sim 94$  km s $^{-1}$  at the north-western end of the linear feature to  $\sim 100$  km s $^{-1}$  at the south-eastern end. The small cluster of maser spots north of the south-eastern end has a velocity of  $\sim 95$  km s $^{-1}$ . The 1.3 cm image (Figure 4c), with 20 $\times$  higher angular resolution than the 7 mm image (Figure 4a), shows the OH masers situated along the south-western boundary of the continuum source, at the edge of the CH<sub>3</sub>CN emission (Figure 4d). The location of the OH masers suggests that they arise within a molecular shell surrounding the ionized gas.

The OH maser velocities in G28.20 N roughly agree with the CH<sub>3</sub>CN velocity of  $\sim 95$ –96 km s $^{-1}$ ; however, they are redshifted relative to the H II region velocity of  $\sim 93$  km s $^{-1}$  estimated by the systemic velocity of the highest frequency RRL observed toward G28.20 N (H30 $\alpha$  at 1.3 mm, Keto et al. 2008; Welch & Marr 1987). A similar redshift is seen for CH<sub>3</sub>OH masers, detected over the velocity range 94 – 105 km s $^{-1}$ . These redshifts for OH and CH<sub>3</sub>OH masers, together with the fact that they appear projected against the optically thick continuum, suggest that they arise on the near side of G28.20 N, thus supporting the scenario that the masers are located in a collapsing molecular envelope surrounding the H II region. A similar scenario was proposed for W3(OH) (Reid et al. 1980) and several other UC H II regions (including G34.26 C, and G45.07 NE; Garay et al. 1985) based on the maser and radio continuum emission in those regions. This interpretation can also apply to G10.96 W from our sample, where the two CH<sub>3</sub>OH maser spots are near the continuum emission peak, and have velocities ( $\sim 25$  km s $^{-1}$ ; Walsh et al. 1998) redshifted by  $\sim 14$  km s $^{-1}$  relative to the H66 $\alpha$  velocity (see Table 7).

The OH maser velocities in G28.20 N appear to be inconsistent with the velocity gradient reported for the H53 $\alpha$  line by Sewilo et al. (2008). In particular, the H53 $\alpha$  velocity gradient, when extrapolated to the position of the arc of maser emission, gives velocities of 115 – 120 km s $^{-1}$ , significantly higher than the OH maser velocities of 93 – 101 km s $^{-1}$ . The differing direction and magnitude of the H53 $\alpha$  and the OH velocity gradients suggests that dynamics of the ionized and molecular gas trace different phenomena.

The orientation of the H<sub>2</sub>O masers (SE-NW) in G28.20 N is consistent with the outflow suggested by Sewilo et al. (2008) and Qin et al. (2008). However, the velocity structure of the masers is ambiguous and does not provide strong evidence for the outflow.

In G45.07 NE, the H<sub>2</sub>O maser spots are aligned spatially and kinematically with the outflow axis detected in CO(6-5) and CS(2-1) molecular lines (Hofner & Churchwell 1996; see Section 4.4), suggesting that the masers form in warm and dense shocked gas at the inner edges of the outflow lobes (Hunter et al. 1997).

#### 5.4. *Spitzer*/IRAC Mid-IR Emission

We find that all the radio components have point source counterparts in the GLIMPSE Archive except G34.26 A and B, and G45.07 SW. A faint mid-IR source was detected at the position of G45.07 SW; however, it was not included in the GLIMPSE catalog due to the close proximity of a much brighter source (G45.07 NE) that prevented an accurate photometric measurement. G34.26 A does not have a clear counterpart in the IRAC image; this source was detected in the mid-IR by earlier studies, unlike component B which is undetected in the mid-IR.

In Table 10, we list GLIMPSE counterparts to the radio sources (the closest neighbors). The distance between the mid-IR and radio positions ranges from 0''.2 for G45.07 NE to 2''.4 for G28.20 S (see Table 10). The proximity of the mid-IR sources to the radio peaks of HC H II regions suggests that these sources probably are the ionizing (proto)stars.

The relatively low density of stars nearby to G10.96 E and G28.20 relative to more distant parts of these fields, suggests extinction of background stars in these regions. The majority of IR sources shown in Figures 7-10 are probably background stars; however, we expect to find a number of young stellar objects (YSOs) in these MSFRs. The YSOs can be identified by their mid-IR colors and by fitting their spectral energy distributions with YSO models. This would be particularly interesting for G28.20, which is located in an IRDC (see Figure 8).

The *Spitzer* images of the sources from our sample suggest that generally the large-scale spatial distribution of gas and dust in these regions are similar; G34.26 C being the principal exception in our sample. Higher resolution infrared observations would be worthwhile, however, to separate diffuse emission from the mid-IR emission from outflows and disks (e.g., NGC7538 IRS 1; De Buizer & Minier 2005).

## 6. Summary

We present high spatial resolution ( $0.^{\prime\prime}9$  to  $2.^{\prime\prime}3$ ), multi-transition ( $\text{H}53\alpha$  to  $\text{H}92\alpha$ ) Very Large Array observations of four massive star formation regions hosting HC H II region candidates identified in earlier studies. G10.96, G28.20, and G34.26 contain HC H II region candidates with broad  $\text{H}92\alpha$  (G10.96 W, G28.20 N) or  $\text{H}76\alpha$  (G34.26 B) lines (Sewilo et al. 2004a). An additional HC H II region candidate (G45.07 NE), known to have broad  $\text{H}66\alpha$  and  $\text{H}76\alpha$  lines, small size, high electron density and emission measure, was also included in this survey. We observed up to two additional transitions per source to investigate the change of line width with frequency. We found a strong correlation of line width with principal quantum number, i.e., higher frequency lines of sources with broad  $\text{H}92\alpha$  or  $\text{H}76\alpha$  lines have narrower linewidths ( $<40 \text{ km s}^{-1}$ ) indicating that pressure broadening is the main line broadening mechanism at lower frequencies. This result is not surprising because of the high electron density in HC H II regions. However, large scale dynamics is also an important contributor to line broadening (Sewilo et al. 2008). We determined physical properties of the H II regions based on both the continuum and line data. Multi-frequency RRLs reported in this paper are well-separated in principal quantum number and will provide good constraints for non-LTE models of these regions.

We also present a comparison of the radio continuum and mid-IR emission in HC H II regions from our sample. Based on the *Spitzer* GLIMPSE survey, covering a wavelength range from 3.6 to  $8.0 \mu\text{m}$ , we find a generally good correspondence between the radio continuum and dust distributions for the sources in our sample. The mid-IR images, however, show more complex features and reveal multiple sources that do not correspond so well to the radio continuum.

We report the distribution of  $\text{H}_2\text{O}$ ,  $\text{OH}$ , and  $\text{CH}_3\text{OH}$  masers with respect to the radio continuum. We also present high-resolution VLA archival data for the water masers in G28.20 N for the first time. We compile information from the literature on maser emission in G10.96, G28.20, and G45.07. A detailed discussion of the maser distribution in G34.26 can be found elsewhere (e.g., Hofner & Churchwell 1996, Gasiprong et al. 2002). As expected, all of the massive star formation regions studied in this paper are associated with maser emission; however, the masers are not coincident with all the radio components in these regions. In G10.96, G28.20, and G45.07 the masers are associated only with the HC H II regions (G10.96 W, G28.20 N, G45.07 NE). In G34.26 the masers are coincident with both the HC H II region G34.26 B and also with the cometary UC H II region G34.26 C. All of the sources associated with masers have broad RRLs.

The question of the origin of BRRLs is not fully answered, although our observations show that pressure broadening is an important mechanism. To distinguish the effects of

pressure broadening from large scale motions of the gas and at the same time resolve the structures of HC H II regions will require high-resolution observations of millimeter RRLs such as H42 $\alpha$  and H30 $\alpha$ . With its high spatial resolution and sensitivity, ALMA will be the instrument to address this issue.

## 7. Acknowledgements

MS acknowledges the support from the NASA ADP grant NNX10AD43G. EC acknowledges partial support from NSF grant AST-080811. PH acknowledges partial support from NSF grant AST-0908901. We thank Thushara Pillai for useful discussion on the water masers in G28.20–0.04. We also thank an anonymous referee for comments and suggestions that improved the manuscript.

## REFERENCES

- Allamandola L. J., Tielens A. G. G. M., & Barker, J. R. 1989, *Ap. J. Suppl.* 71, 733.
- Altenhoff W. J., Mezger P. G., Wendker H., Westerhout G. 1960, *Veröff Sternwärte Bonn*, No. 59, 48
- Araya, E., Hofner, P., Churchwell, E. & Kurtz, S. 2002, *ApJS*, 138, 63
- Argon, A. L., Reid, M. J., & Menten, K. M. 2000, *ApJS*, 129, 159
- Avalos, M., Lizano, S., Rodríguez, L. F., Franco-Hernández, R., Moran, J. M. 2006, *ApJ*, 641, 406
- Avalos, M., Lizano, S., Franco-Hernández, R., Rodríguez, L. F., & Moran, J. M. 2009, *ApJ*, 690, 1084
- Becker, R. H., White, R. L., Helfand, D. J., & Zoonematkermani, S. 1994, *ApJS*, 91, 347
- Beltrán, M. T., et al. 2004, *ApJ*, 601, L187
- Beltrán, M. T., Cesaroni, R., Neri, R., Codella, C., Furuya, R. S., Testi, L., & Olmi, L. 2005, *A&A*, 435, 901
- Beltrán, M. T., Cesaroni, R., Codella, C., Testi, L., Furuya, R. S., & Olmi, L. 2006, *Nature*, 443, 427
- Beltrán, M., Cesaroni, R., Moscadelli, L., & Codella, C. 2007, *A&A*, 471, L13
- Benjamin, R. A., et al. 2003, *PASP*, 115, 953
- Brocklehurst, M., & Seaton, M. J. 1972, *MNRAS*, 157, 179
- Bronfman, L., Nyman L.-A., May, J. 1996, *A&AS*, 115, 81
- Campbell, M. F., Garland, C. A., Deutsch, L. K., Hora, J. L., Fazio, G. G., Dayal, A., & Hoffmann, W. F. 2000, *ApJ*, 536, 816
- Carey, S. J., et al. 2009, *PASP*, 121, 76
- Caswell, J. L., Vaile, R. A., Ellingsen, S. P., Whiteoak, J. B., & Norris, R. P. 1995, *MNRAS*, 272, 96
- Caswell, J. L., & Vaile, R. A. 1995, *MNRAS*, 273, 328

- Caswell, J. L. 2001, MNRAS, 326, 805
- Caswell, J. L. 2003, MNRAS, 341, 551
- Cesaroni, R., Walmsley, C. M., Kompe, C., & Churchwell, E. B. 1991, A&A, 252, 278
- Churchwell, E., Babler, B. L., Meade, M. R., Whitney, B. A., Benjamin, R., Indebetouw, R., Cyganowski, C., Robitaille, T. P., Povich, M., Watson, C., Bracker, S. 2009, PASP, 121, 213
- Codella, C., Palumbo, G. G. C., Pareschi, G., Scappini, F., Caselli, P., & Attolini, M. R. 1995, MNRAS, 276, 57
- Codella, C., Testi, L., & Cesaroni, R. 1997, A&A, 325, 282
- Crowther, P. A., & Conti, P. S. 2003, MNRAS, 343, 143
- Cyganowski, C. J., et al. 2008, AJ, 136, 2391
- Cyganowski, C. J., Brogan, C. L., Hunter, T. R., Churchwell, E. 2009, ApJ, 702, 1615
- De Buizer, J. M., Radomski, J. T., Telesco, C. M., & Pina, R. K. 2003, ApJ, 598, 1127
- De Buizer, J. M., Radomski, J. T., Telesco, C. M., & Pina, R. K. 2005, ApJS, 156, 179
- De Pree, C. G., Gaume, R. A., Goss, W. M., & Claussen, M. J. 1996, ApJ, 464, 788
- De Pree, C. G., Mehringer, D. M., & Goss, W. M. 1997, ApJ, 482, 307
- Elitzur, M., de Jong, T. 1978, A&A, 67, 323
- Fazio, G. G., et al. 2004, ApJS, 154, 10
- Fey, A. L., Gaume, R. A., Nedoluha, G. E., & Claussen, M. J. 1994, ApJ, 435, 738
- Fish, V. L., Reid, M. J., Wilner, D. J., & Churchwell, E. 2003, ApJ, 587, 701
- Forster, J. R., & Caswell, J. L. 1989, A&A, 213, 339
- Franco, J., Kurtz, S., Hofner, P., Testi, L., García-Segura, G., & Martos, M. 2000, ApJ, 542, L143
- Furuya, R. S., et al. 2002, A&A, 390, L1
- Garay, G., Reid, M. J., & Moran, J. M. 1985, ApJ, 289, 681

- Garay, G., & Rodríguez, L. F., 1990 ApJ, 362, 191
- Garay, G., Rodríguez, L. F. & van Gorkom, J. H. 1986, ApJ, 309, 553
- Gasiprong, N., Cohen, R. J., & Hutawarakorn, B. 2002, MNRAS, 336, 47
- Gaume, R. A. & Mutel, R. L. 1987 ApJS, 65, 193
- Han, F., Mao, R. Q., Lu, J., Wu, Y. F., Sun, J., Wang, J. S., Pei, C. C., Fan, Y., Tang, G. S., Ji, H. R. 1998, A&AS, 127, 181
- Hatchell, J., Fuller, G. A., & Millar, T. J. 2001, A&A, 372, 281
- Heaton, B. D., Little, L. T., & Bishop, L. S., A&A, 213, 148
- Hoare, M. G., Kurtz, S. E., Lizano, S., Keto, E., & Hofner, P., 2007 in Protostars & Planets V, ed. B. Reipurth, D. Jewitt, & K. Keil, (Tucson: University of Arizona Press), 181
- Hofner, P., & Churchwell, E. 1996, A&AS, 120, 283
- Hollenbach, D., Johnston, D., Lizano, S., & Shu, F. 1994, ApJ, 428, 654
- Hunter, T. R., Phillips, T. G., Menten, K. M. 1997, ApJ, 478, 283
- Ignace, R., & Churchwell, E. 2004, ApJ, 610, 351
- Keto, E., Proctor, D., Ball, R., Arens, J., & Jernigan, G. 1992, ApJ, 401, L113
- Keto, E. 2003, ApJ, 599, 1196
- Keto, E., Zhang, Q., & Kurtz, S. 2008, ApJ, 672, 423
- Klaassen, P. D., Wilson, C. D., Keto, E. R., & Zhang, Q. 2009, ApJ, 703, 1308
- Kraemer, K. E., et al. 2003, ApJ, 588, 918
- Kurtz, S., Churchwell, E., & Wood, D. O. S. 1994, ApJS, 91, 659
- Kurtz, S., Cesaroni, R., Churchwell, E., Hofner, P., & Walmsley, C. M. 2000, in “Protostars and Planets IV”, ed. V. Mannings, A. Boss, & S. Russell (Tucson: University of Arizona Press), 299
- Kurtz, S., Hofner, P., & Vargas Alvares, C. 2004, ApJS, 155, 149
- Kurtz, S. 2005, ”Massive Star Birth: A Crossroads of Astrophysics”, IAU Symposium 227, eds. R. Cesaroni, M. Felli, E. Churchwell, & M. Walmsley, p. 111

- Kurtz, S., & Hofner, P. 2005, ApJ, 130, 711
- Lizano, S., Canto, J., Garay, G., & Hollenbach, D. 1996, ApJ, 468, 739
- Lugo, J., Lizano, S., & Garay, G. 2004, ApJ, 614, 807
- Matthews, N., Little, L. T., MacDonald, G. H., Andersson, M., Davies, S. R., Riley, P. W., Dent, W. R. F., & Vizard, D. 1987, A&A, 184, 284
- Meade, M., Whitney, B. A., Babler, B., Indebetouw, R., Bracker, S., Cohen, M., Robitaille, T., Benjamin, R., & Churchwell, E. 2009, GLIMPSE documentation available at the *Spitzer* Science Center (<http://ssc.spitzer.caltech.edu/spitzermission/observingprograms/legacy/glimpse/>)
- Menten, K. M. 1991, ApJ, 380, L75
- Mezger, P. G., & Henderson, A. P. 1967, ApJ, 147, 471
- Mookerjea, B., Casper, E., Mundy, L. G., & Looney, L. W. 2007, ApJ, 659, 447
- Moscadelli, L., Goddi, C., Cesaroni, R., Beltrán, M. T., & Furuya, R. S. 2007, A&A, 472, 867
- Oster, L. 1961, Reviews of Modern Physics, 33, 525
- Panagia, N., & Walmsley, C. M. 1978, A&A, 70, 411
- Plume, R., Jaffe, D. T., Evans, N. J., II, Martín-Pintado, J., & Gómez-González, J. 1997, ApJ, 476, 730
- Povich, M. S., Stone, J. M., Churchwell, E., Zweibel, E. G., Wolfire, M. G., Babler, B. L., Indebetouw, R., Meade, M. R., & Whitney, B. A. 2007, ApJ, 660, 346
- Price, S. D., Egan, M. P., Carey, S. J., Mizuno, D., Kuchar, T. 2001, A&A, 121, 2819
- Purcell, C. R., Hoare, M. G., & Diamond, P. 2008, “Massive Star Formation: Observations Confront Theory”, eds. H. Beuther, H. Linz, & T. Henning, ASP Conference Series, Vol. 387, p. 389
- Qin, S.-L., Huang, M., Wu, Y., Xue, R., & Chen, S. 2008, ApJ, 686, 21
- Reid, M. J., Haschick, A. D., Burke, B. F., Moran, J. M.; Johnston, K. J., & Swenson, G. W., Jr. 1980, ApJ, 239, 89
- Reid, M. J., & Ho, P. T. P. 1985, ApJ, 288, L17

- Rohlfs, K., & Wilson, T. L. 1986, “Tools of Radio Astronomy”, 2nd edition, Springer-Verlag Berlin Heidelberg
- Roelfsema, P. R., & Goss, W. M. 1992, A&ARv, 4, 161
- Schutte, A. J., van der Walt, D. J., Gaylard, M. J., & MacLeod, G. C. 1993, MNRAS, 261, 783
- Sellgren K. 1984, ApJ, 277, 623
- Sewiło, M., Churchwell, E., Kurtz, S., Goss, W. M., & Hofner, P. 2004a, ApJ, 605, 285 (Paper I)
- Sewiło, M., Watson, C., Araya, E., Churchwell, E., Hofner, P., & Kurtz, S. 2004b, ApJS, 154, 553
- Sewiło, M., Churchwell, E., Kurtz, S., Goss, W. M., & Hofner, P. 2008, ApJ, 681, 350
- Smith, L. J., Norris, R. P. F., & Crowther, P. A. 2002, MNRAS, 337, 1309
- Sollins, P. K., Zhang, Q., Keto, E., & Ho, P. T. P. 2005, ApJ, 631, 399
- Tan, J. C., & McKee, C. F. 2003, *ASP Conference Series 221*, also astro-ph/0309139
- Tielens A. G. G. M., et al. 1993, Science 262, 86
- Turner, B. E., & Matthews, H. E. 1984, ApJ, 277, 164
- Voit, G. M 1992, MNRAS, 258, 841
- Walsh, A. J., Hyland, A. R., Robinson, G., & Burton, M. G. 1997, MNRAS, 291, 261
- Walsh, A. J., Burton, M. G., Hyland, A. R., & Robinson, G. 1998, MNRAS, 301, 640
- Welch, W. J., & Marr, J. 1987, ApJ, 317, L21
- Wilcots, E. M., Brinks, E., & Higdon, J. 2003, “*A Guide for VLA Spectral Line Observers*”, <http://www.vla.nrao.edu/astro/guides/sline/current/>
- Wood, D. O. S., & Churchwell, E. 1989, ApJS, 69, 831

Table 1. Instrumental Parameters for the VLA Observations

Parameter	2003 Mar 20	2004 Mar 7, 8 <sup>a</sup>
Program .....	AS753	AS797
Transitions observed .....	H53 $\alpha$ ... ...	a) H66 $\alpha$ b) H76 $\alpha$ c) H92 $\alpha$
Observed sources .....	G28.20−0.04 G34.26+0.15 ...	G10.96+0.01 (ab) G28.20−0.04 (b) G45.07+0.13 (c)
Total observing time .....	10 hr ... ...	a) 3 hr b) 9 hr c) 1 hr
Configuration <sup>b</sup> .....	D	C
Synthesized beam/FWHM (''), PA( $^{\circ}$ ):		
G10.96+0.01 .....	...	1.4 $\times$ 0.8, −8 (a) 2.0 $\times$ 1.2, −2 (b)
G28.20−0.04 .....	1.9 $\times$ 1.4, −10	1.5 $\times$ 1.4, −10 (b)
G34.26+0.15 .....	1.6 $\times$ 1.5, −4	...
G45.07+0.13 .....	...	2.5 $\times$ 2.4, −31 (c)
Rest frequency of the H line .....	42,951.97 MHz ... ...	a) 22,364.17 MHz b) 14,689.99 MHz c) 8,309.38 MHz
Observing mode .....	1A	2AD
Bandwidth .....	25 MHz	12.5 MHz
Number of channels .....	31	31
Channel separation .....	781.25 kHz	390.625 kHz
Velocity resolution <sup>c</sup> .....	6.5 km s <sup>−1</sup> ... ...	a) 6.2 km s <sup>−1</sup> b) 9.6 km s <sup>−1</sup> c) 16.9 km s <sup>−1</sup>
Flux density calibrator (Jy):		
<u>3C 286</u> for G10.96+0.01 .....	...	2.53 (a), 3.50 (b)
G28.20−0.04 .....	1.47	3.50 (b)
G34.26+0.15 .....	1.47	...
G45.07+0.13 .....	...	5.27 (c)
Phase calibrators (Jy):		
<u>1820−254</u> for G10.96+0.01 .....	...	0.610 $\pm$ 0.004 (a) 0.692 $\pm$ 0.003 (b)
<u>1851+005</u> for G28.20−0.04 .....	0.75 $\pm$ 0.02	0.917 $\pm$ 0.003 (b)
G34.26+0.15 .....	0.72 $\pm$ 0.02	...

Table 1—Continued

Parameter	2003 Mar 20	2004 Mar 7, 8 <sup>a</sup>
<u>1925+211</u> for G45.07+0.13 .....	...	2.57 ± 0.01 (c)

<sup>a</sup>a, b, and c indicate values for the H66 $\alpha$ , H76 $\alpha$ , and H92 $\alpha$  lines, respectively.

<sup>a</sup>Primary beams are: 1' for AS753; 2', 3', and 5.4' for AS797 (a), (b), and (c), respectively.

<sup>c</sup>The observations were done with uniform spectral weighting, thus the velocity resolution is 1.2 times the channel separation.

Table 2. Transitions Observed toward Individual Sources and Adopted Distances

Source	H53 $\alpha$	H66 $\alpha$	H76 $\alpha$	H92 $\alpha$	D (kpc)	Ref.
G10.96+0.01 .....	...	+	+	+	14.0 <sup>+1.3</sup> <sub>-0.9</sub>	1
G28.20-0.04 .....	+	...	+	+	5.7 <sup>+0.5</sup> <sub>-0.8</sub>	2
G34.26+0.15 .....	+	...	+	...	3.7	3
G45.07+0.13 .....	...	...	...	+	6.0	3

Note. — The plus signs (+) indicate the observed transitions.

<sup>a</sup>Transitions reported in Sewiło et al. (2004)

References. — (1) Sewiło et al. 2004a; (2) Fish et al. 2003; (3) Araya et al. 2002

Table 3. Continuum Parameters<sup>a</sup>

Source	$\lambda$	Comp.	Position		Time on Source (h)	Source Diameter $\theta_{maj} \times \theta_{min}$ ('' $\times$ '')	Source PA <sup>a</sup> (°)	Integrated Flux Density (mJy)		RMS in Image (mJy beam $^{-1}$ )
			$\alpha(J2000)$ (h m s)	$\delta(J2000)$ ( $^{\circ}$ ' '')						
G10.96+0.01 ...	1.3 cm	E <sup>b</sup>	18 09 42.85	-19 26 29.6	0.5	...	...	...	...	0.4
		W	18 09 39.35	-19 26 28.1	...	1.0 $\times$ 0.9	177	291	...	...
	2 cm	E/E1 <sup>b</sup>	18 09 42.98	-19 26 28.2	1.4	...	...	...	...	0.4
	...	E/E2 <sup>b</sup>	18 09 42.85	-19 26 30.0	...	...	...	...	...	...
G28.20-0.04 ...	0.7 cm	N	18 42 58.11	-04 13 57.5	0.6	0.7 $\times$ 0.5	159	710	1.4	...
		S	18 42 58.12	-04 14 04.9	...	2.9 $\times$ 2.4	177	<108 <sup>c</sup>	...	
		S1	18 42 58.29	-04 14 04.4	...	...	...	...	...	
	2 cm	N	18 42 58.11	-04 13 57.4	2.6	0.8 $\times$ 0.6	150	494	0.4	...
		S	18 42 58.13	-04 14 04.7	...	2.9 $\times$ 2.7	28	132	...	
	0.7 cm	A	18 53 18.79	+01 14 56.3	1.0	0.3 $\times$ 0.2	54	>86 <sup>d</sup>	2.8	...
G34.26+0.15 ...	0.7 cm	B <sup>e</sup>	18 53 18.66	+01 15 00.5	...	...	...	...	...	
		C <sup>f</sup>	18 53 18.56	+01 14 58.2	...	...	...	6000 <sup>g</sup>	...	
G45.07+0.13 ...	3.6 cm	NE	19 13 22.08	+10 50 53.2	0.6	0.6 $\times$ 0.6	87	350	0.8	...
		SW	19 13 21.83	+10 50 48.2	...	1.4 $\times$ 1.1	82	60	...	

<sup>a</sup>Source positions, deconvolved angular sizes, position angles, and integrated flux densities were determined by elliptical Gaussian fitting using the AIPS routine JMFIT. We estimate the positional uncertainty to be  $\sim 0''.1$ . Uncertainties in source sizes depend on both the brightness and the intrinsic source extent; we estimate them to be accurate to within  $\sim 10\%$ . The flux density uncertainties are 10% - this value takes into account the error of the fit (JMFIT) and systematic effects (e.g. calibration errors, mismatches between the Gaussian model and the actual source shape, etc.).

<sup>b</sup>The E component of the MSFR G10.96 is overresolved at both 1.3 and 2 cm. Most of the flux is filtered out, thus we do not give either the total flux density or source size at these wavelengths. The 1.3 cm coordinates correspond to the maximum pixel. The peak flux density at 1.3 cm is 3.9 mJy beam $^{-1}$ . The 2 cm flux density from the region that encloses two compact components (9  $\sigma$  level; see Fig. 2b) is  $38 \pm 3$  mJy beam $^{-1}$ .

<sup>c</sup>The faint S1 component emerging at 7 mm is partially blended with component S; the reported flux density is the total integrated flux density from both components. The flux density of the S1 component constitutes  $\sim 15\%$  of the total flux. The peak 7 mm flux density of S1

is 26.6 mJy beam<sup>-1</sup>.

<sup>d</sup>The A component is partially blended with component C; the integrated flux density should be considered the lower limit.

<sup>e</sup>The B component is not fully resolved from the cometary component C, thus we cannot give either its angular diameter or flux density. The position given in the table was determined from the 3.6 cm continuum map in Sewilo et al. (2004).

<sup>f</sup>The coordinates correspond to the maximum pixel in the cometary component C. The peak flux density is 2.78 Jy beam<sup>-1</sup>.

<sup>g</sup>The integrated flux density was calculated using the AIPS task IMEAN from the area of  $\sim 22''$  by  $\sim 12''$  in R.A. and decl., respectively, that encloses all three components of the G34.26 H II region complex. The total flux density of the A component is  $\sim 92$  mJy, the remaining  $\sim 5908$  Jy arise from components B and C. Only a small fraction of this flux density (< 3%) comes from the B component (see text).

Table 4. Positions and Observed Parameters of Water Masers in G28.20–0.04 N

water maser	$\alpha(J2000)$ (h m s)	$\delta(J2000)$ ( $^{\circ}$ ' '')	$v_{LSR}^a$ (km s $^{-1}$ )	$S_{peak}^b$ (Jy)
1	18 42 58.07	-04 13 56.9	97.7	1.2
2	18 42 58.12	-04 13 57.8	95.6	10.7
3	18 42 58.11	-04 13 57.6	93.1	1.6
4	18 42 58.06	-04 13 57.0	91.0	22.2

<sup>a</sup>The velocity of the peak channel.

<sup>b</sup>The uncertainties of peak flux densities are dominated by systematic errors. We adopt a standard 10% uncertainty for the VLA at K-band.

Table 5. Source Averaged Physical Parameters based on Continuum Observations<sup>a</sup>

Source		diameter		$\tau_c$	$n_{e,rms}/10^4$	EM/ $10^7$	U	$M_{HII}$	$\log N'_c$	Spectral <sup>b</sup>
	$\lambda$	(cm)	of sphere (mpc)		( $cm^{-3}$ )	(pc $cm^{-6}$ )	(pc $cm^{-2}$ )	( $M_\odot$ )	( $s^{-1}$ )	Type
G10.96+0.01 <sup>c</sup>	W	1.3	121	0.02	2.9	5.3	57.6	0.6	48.8	O7.5V
.....	...	2	124	0.06	2.7	5.3	56.4	0.6	48.8	...
G28.20−0.04	N	0.7	28	0.04	17	36	43.9	0.05	48.4	O8V
.....	...	2	35	0.2	9.8	19	37.1	0.05	48.2	...
.....	S	0.7	131	0.0003	0.7	0.3	23.4	0.2	47.6	O9.5V
.....	...	2	120	0.01	0.8	0.4	23.9	0.2	47.6	...
G34.26+0.15 <sup>d</sup>	A	0.7	8	0.03	27	24	16.3	0.002	47.1	B0.5V
G45.07+0.13	NE	3.6	32	0.7	9.4	19	33.4	0.04	48.1	O8.5V
.....	SW	3.6	65	0.03	1.4	0.8	18.7	0.05	47.3	B0V

Note. — The physical parameters are: the linear diameter of a spherical H II region (assumed model), the continuum optical depth ( $\tau_c$ ), the rms electron density ( $n_{e,rms}$ ), the emission measure (EM), the excitation parameter (U), the mass of ionized gas ( $M_{HII}$ ), and the Lyman continuum photon flux required to maintain ionization of the nebula ( $N'_c$ ).

<sup>a</sup>We estimate an uncertainty of the derived physical parameters to be up to 20%. These parameters depend on the different combinations of the integrated flux density, observed source size, and assumed distance. All of these quantities have uncertainties of  $\sim 10\%$ .

<sup>b</sup>Lower limits to the spectral types of the exciting stars are derived from  $N'_c$  using the model stellar atmosphere results of Smith et al. (2002). See text for details.

<sup>c</sup>We do not report the physical parameters for component E of G10.96+0.01, because most of the emission from this source is filtered out. See footnotes to Table 3.

<sup>d</sup>We do not report the physical parameters for components B and C of G34.26+0.15. They are blended at our spatial resolution, hence we cannot determine their angular sizes or flux densities.

Table 6. Peak Values of the Physical Parameters<sup>a</sup>

Source		$\nu$ (GHz)	$S_{\nu,peak}$ (mJy/beam)	$\Delta s$ (pc)	$T_B$ (K)	$\tau_c$	$EM/10^7$ (pc cm $^{-6}$ )	$N_{e,rms}/10^4$ (cm $^{-3}$ )
G10.96+0.01	W	22.4	$147.2 \pm 0.4$	0.07	325	0.03	7.1	3.3
.....	...	14.7	$188.6 \pm 0.4$	0.07	460	0.05	4.2	2.4
.....	E	22.4	$3.9 \pm 0.4$	...	9	>0.001	0.2	...
.....	E1 <sup>b</sup>	14.7	$6.5 \pm 0.4$	...	16	0.002	0.1	...
.....	E2 <sup>b</sup>	14.7	$6.9 \pm 0.4$	...	17	0.002	0.1	...
G28.20−0.04	N	42.9	$651 \pm 1$	0.015	165	0.017	14.4	9.8
.....	...	14.7	$401.9 \pm 0.4$	0.02	1079	0.1	10.1	7.3
.....	S	42.9	$27 \pm 1$	0.07	7	>0.001	0.6	0.9
.....	...	14.7	$30.7 \pm 0.4$	0.08	82	0.01	0.7	1.0
G34.26+0.15	A	42.9	$86 \pm 3$	0.004	24	0.002	2.1	7.1
.....	B	42.9	$120^c \pm 3$	...	33	0.003	2.9	...
.....	C	42.9	$2777 \pm 3$	...	773	0.1	69.7	...
G45.07+0.13	NE	8.3	$328.3 \pm 0.7$	0.02	988	0.1	2.7	4.0
.....	SW	8.3	$49.4 \pm 0.7$	0.04	149	0.02	0.4	1.1

<sup>a</sup>We estimate an uncertainty of the derived physical parameters to be up to 20%. These parameters depend on combinations of the integrated flux density, observed source size, and assumed distance. All of these quantities have uncertainties of order 10%.

<sup>b</sup>Two maxima/subcomponents can be distinguished in the 2 cm image of component E of G10.96+0.01 (see Fig. 2). E1 and E2 correspond to the NE and SW maxima, respectively.

<sup>c</sup>The peak flux density of G34.26+0.15 component B is an upper limit because of blending with component C.

Table 7. Gaussian Fits to the H53 $\alpha$ , H66 $\alpha$ , H76 $\alpha$ , and H92 $\alpha$  Radio Recombination Lines

Source	RRL	$V_{\text{LSR}}$ (km s $^{-1}$ )	FWHM <sup>a</sup> (km s $^{-1}$ )	$S_L$ (mJy)	$S_C^b$ (mJy)	$\frac{S_L}{S_C}$ (peak)	$\int \frac{S_L}{S_C} dv$ (km s $^{-1}$ )
G10.96+0.01 .	E	H66 $\alpha$ <sup>c</sup>	$11.4 \pm 0.7$	$18.7 \pm 1.8$	$12.6 \pm 1.0$	$46.3 \pm 2.3$	$0.27 \pm 0.03$
	...	H76 $\alpha$ <sup>c</sup>	$15.8 \pm 1.0$	$25.3 \pm 2.5$	$9.7 \pm 0.8$	$53.8 \pm 2.7$	$0.18 \pm 0.02$
	W	H66 $\alpha$	$13.6 \pm 0.4$	$28.5 \pm 1.0$	$35.9 \pm 1.1$	$147 \pm 7$	$0.24 \pm 0.01$
	...	H76 $\alpha$	$13.3 \pm 0.5$	$29.6 \pm 1.3$	$19.9 \pm 0.7$	$131 \pm 7$	$0.15 \pm 0.01$
G28.20−0.04 .	N	H53 $\alpha$	$88.5 \pm 0.5$	$39.0 \pm 1.4$	$144 \pm 4$	$372 \pm 19$	$0.39 \pm 0.02$
	...	H76 $\alpha$	$80.1 \pm 0.8$	$55.7 \pm 2.2$	$17.0 \pm 0.5$	$235 \pm 12$	$0.07 \pm 0.01$
	S	H53 $\alpha$	$99.6 \pm 0.4$	$19.9 \pm 0.9$	$63.6 \pm 2.4$	$65.3 \pm 3.3$	$0.97 \pm 0.06$
	...	H76 $\alpha$	$99.3 \pm 0.5$	$24.8 \pm 1.3$	$7.3 \pm 0.3$	$34.9 \pm 1.7$	$0.21 \pm 0.01$
G34.26+0.15 .	A	H53 $\alpha$	$50.2 \pm 0.4$	$21.9 \pm 1.0$	$46.3 \pm 1.7$	$62.9 \pm 3.1$	$0.74 \pm 0.05$
	B	H53 $\alpha$ <sup>c</sup>	$64.9 \pm 1.0$	$34.8 \pm 2.6$	$20.5 \pm 1.2$	$58.6 \pm 2.9$	$0.35 \pm 0.03$
	C	H53 $\alpha$	$47.9 \pm 1.2$	$49.4 \pm 3.7$	$589 \pm 32$	$2587 \pm 129$	$0.23 \pm 0.02$

<sup>a</sup>Full width at half-maximum.

<sup>b</sup> $S_C$  is a continuum flux density of the same area of the source over which a RRL was integrated. It was determined using AIPS task IMEAN.

<sup>c</sup>The spectrum was Hanning smoothed.

Table 8. Corrected H $53\alpha$ , H $66\alpha$ , H $76\alpha$ , and H $92\alpha$  Radio Recombination Line Parameters and the LTE Electron Temperatures

Source	RRL		FWHM <sup>a</sup> (km s <sup>-1</sup> )	( $\frac{S_L}{S_C}$ ) <sup>b</sup> (peak)	T $_e^*$ <sup>c</sup> (K)
G10.96+0.01 .	E	H $66\alpha$	15.5 ± 2.1	...	11400 ± 1600
	...	H $76\alpha$	19.6 ± 3.2	...	8800 ± 1400
	W	H $66\alpha$	27.8 ± 1.1	0.25 ± 0.01	7500 ± 500
	...	H $76\alpha$	28.0 ± 1.4	0.16 ± 0.01	7400 ± 500
G28.20−0.04 .	N	H $53\alpha$	38.5 <sup>d</sup> ± 1.5	0.39 ± 0.02	7000 ± 400
	...	H $76\alpha$	54.9 <sup>d</sup> ± 2.3	0.08 ± 0.01	7300 ± 500
	S	H $53\alpha$	18.8 ± 0.9	...	5900 ± 400
	...	H $76\alpha$	22.9 ± 1.4	...	6800 ± 500
G34.26+0.15 .	A	H $53\alpha$	20.9 ± 1.0	0.75 ± 0.05	6800 ± 500
	B	H $53\alpha$	33.1 ± 2.8	...	8800 ± 900
	C	H $53\alpha$	49.0 ± 3.7	0.24 <sup>e</sup> ± 0.02	8700 ± 800

<sup>a</sup>Full width at half-maximum (FWHM) of the spectral lines corrected for broadening introduced by spectrometer and smoothing. The convolving function in the spectral frequency domain was assumed to be a Gaussian function with FWHM of 1.2 times a channel width (or twice a channel width if a spectrum is Hanning smoothed) and deconvolved from the observed line widths. Velocity resolutions for all frequencies are given in Table 1.

<sup>b</sup>We adopt the same uncertainties as for the fitted line-to-continuum ratios given in Table 7.

<sup>c</sup>For optically thin sources, the values of ( $\frac{S_L}{S_C}$ )<sub>peak</sub> from Table 7 were used to calculate T $_e^*$ .

<sup>d</sup>For G28.20 N, the H $53\alpha$  and H $76\alpha$  line widths are slightly smaller than those reported in Sewiło et al. (2008) based on the same data: 39.7 ± 1.3

km s<sup>-1</sup> and  $57.6 \pm 2.2$  km s<sup>-1</sup> for H53 $\alpha$  and H76 $\alpha$  lines, respectively. The difference in linewidths is due to different integration areas used in both papers. While Sewiło et al. (2008) integrated the lines over the entire source, the lines reported in this paper were integrated over the area enclosed by the 50% contour.

<sup>e</sup>The line-to-continuum ratios corrected for opacity for this source was derived from the peak optical depths listed in Table 6.

Table 9. Flux densities of G28.20-0.04 N

$\nu$ (GHz)	Instr.	Synth. Beam (" $\times$ ")	$S_\nu$ (mJy)	Ref.
5.0	VLA	$2.0 \times 1.6$	$150 \pm 15$	1
6.7	ATCA	$\sim 1.9$	$326^a$	2
8.3	VLA	$0.9 \times 0.8$	$297 \pm 45$	3
8.3	VLA	$4.9 \times 2.7$	$300 \pm 30$	4
14.7	VLA	$1.5 \times 1.4$	$494 \pm 50$	9
14.7	VLA	$0.6 \times 0.5$	$543 \pm 81$	3
22.4	VLA	$0.3 \times 0.2$	$980^{a,b}$	5
22.4	VLA	$0.1 \times 0.1$	$630 \pm 63$	9
43.0	VLA	$1.9 \times 1.4$	$710 \pm 70$	9
43.0	VLA	$0.17 \times 0.13$	$645 \pm 65$	6
231.9	SMA	1	$720^{a,c}$	7
231.9	SMA	$0.6 \times 0.2$	$890 \pm 30^c$	8

<sup>a</sup>Uncertainties are not provided in the referenced papers.

<sup>b</sup>The 1.3 cm flux density given by Sollins et al. (2005) seems to be anomalously high relative to other measurements (see Fig. 12).

<sup>c</sup>Both 231.9 GHz flux densities are from the same SMA observations. Any difference in flux density represents a difference in the data reduction.

References. — (1) Purcell et al. 2008; (2) Walsh et al. 1998 ; (3) Kurtz et al. 1994; (4) Sewiło et al. 2004a; (5) Sollins et al. 2005; (6) Sewiło et al. 2008; (7) Keto et al. 2008; (8) Qin et al. 2008; (9) this paper

Table 10. GLIMPSE Counterparts to the Radio Continuum Sources

Source	GLIMPSE ID <sup>a</sup>	d <sup>b</sup>		Flux densities <sup>c</sup> (mJy)				
		(")	(mpc)	$K_s$	$3.6\mu m$	$4.5\mu m$	$5.8\mu m$	$8.0\mu m$
G10.96 W	SSTGLMA G010.9584+00.0219	2	136	...	$9.7 \pm 0.9$	$59 \pm 8$	$174 \pm 12$	$395 \pm 31$
G10.96 E2	SSTGLMA G010.9646+00.0098	0.3	20	...	$8 \pm 3$	$13 \pm 4$	$59 \pm 8$	...
G28.20 N	SSTGLMA G028.2003-00.0493	2.2	61	$9.0 \pm 0.4$	$358 \pm 19$	$2123 \pm 99$	$3892 \pm 99$	...
G28.20 S	SSTGLMAG028.1984-00.0501	2.4	66	...	$2.1 \pm 0.3$	$9 \pm 1$	...	...
G34.26 C	SSTGLMA G034.2572+00.1533	0.7	13	...	...	$4857 \pm 278$	$4481 \pm 155$	...
G45.07 NE	SSTGLMA G045.0712+00.1321	0.2	6	$40 \pm 1$	$2240 \pm 184$	...	...	...

<sup>a</sup>The Galactic coordinates of the *Spitzer* sources are part of the GLIMPSE IDs.

|  
43

<sup>b</sup>The distance between the radio continuum source and the nearest mid-IR GLIMPSE point source; kinematic distances to MSFRs listed in Table 2 were used to calculate distances in mpc.

<sup>c</sup>None of the sources has J and H fluxes available in the 2MASS Point Source Catalog.

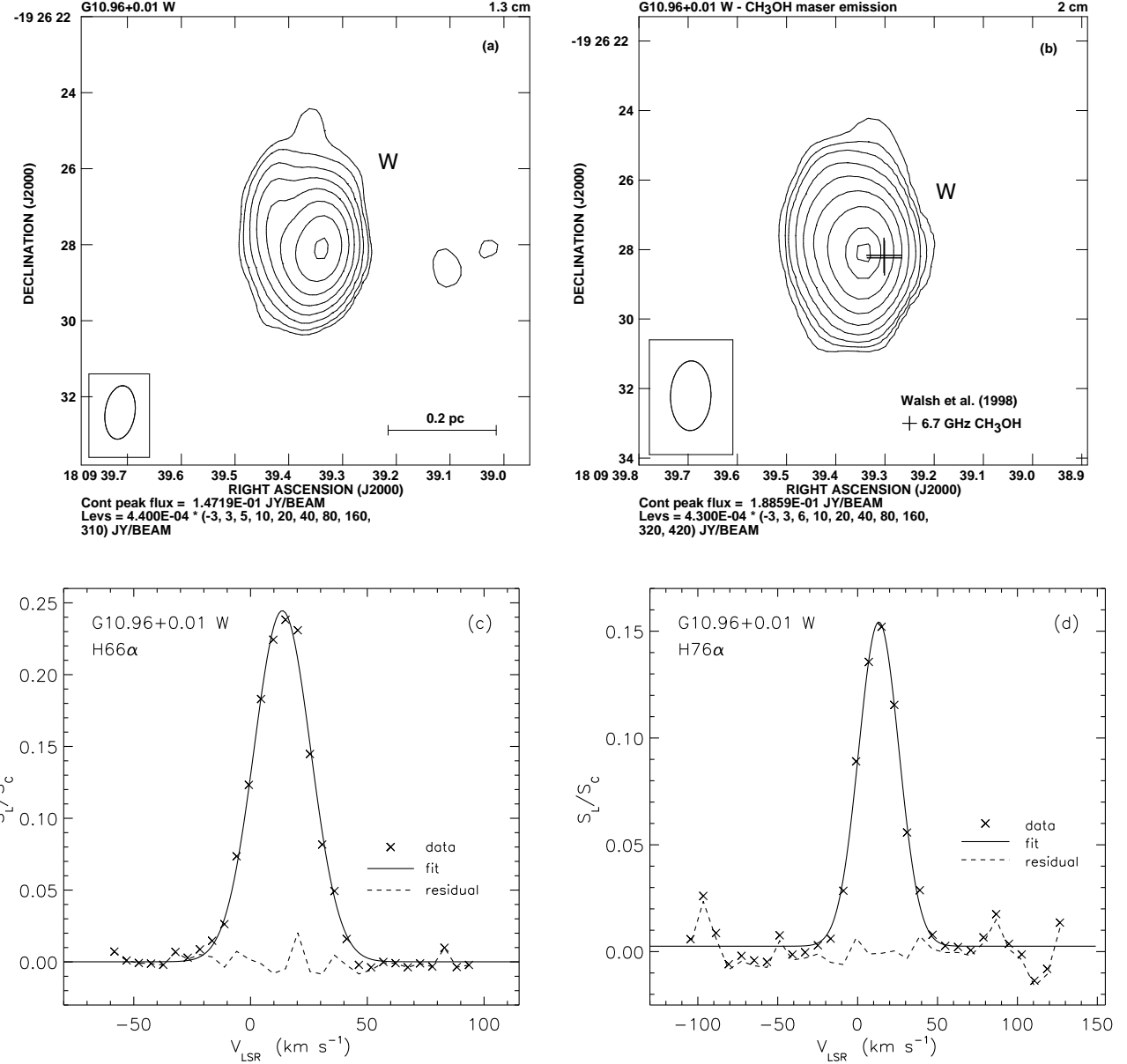


Fig. 1.— The 1.3 (a) and 2 cm (b) VLA continuum images and the H66 $\alpha$  (c) and H76 $\alpha$  (d) line profiles integrated over the central portion of the W continuum component of the MSFR G10.96. The positions of the two CH<sub>3</sub>OH maser spots in G10.96 W are superimposed on the 2 cm image (b). Beam sizes are the same as in Figure 2.

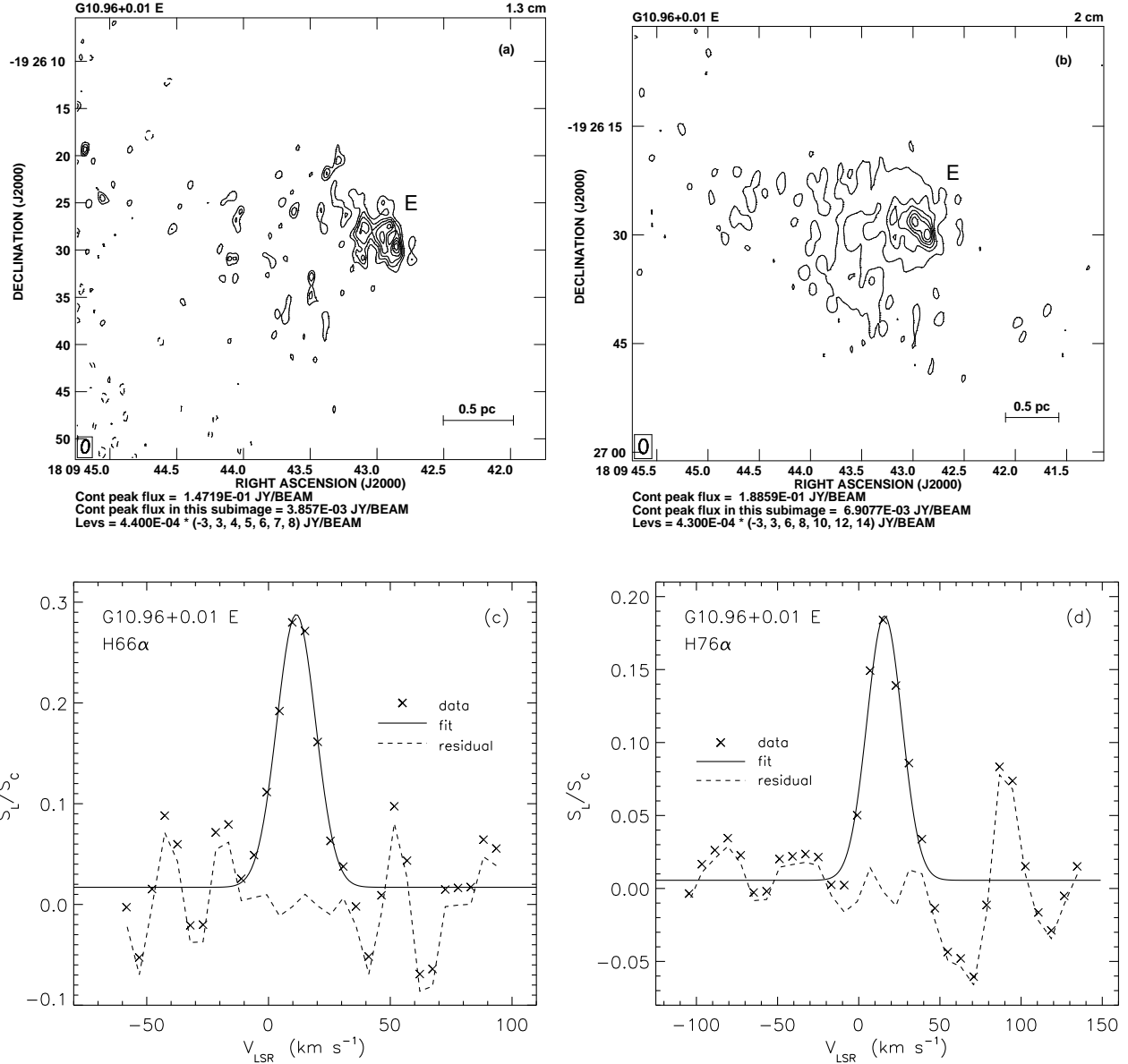


Fig. 2.— The 1.3 (a) and 2 cm (b) VLA continuum images and the H66 $\alpha$  (c) and H76 $\alpha$  (d) line profiles from the E continuum component of the MSFR G10.96. The beam sizes shown in the lower left corners of the continuum images are  $\sim 1.^{\circ}1$  and  $\sim 1.^{\circ}6$  at 1.3 and 2 cm, respectively (see Table 1). The 1.3 cm peak of maximum emission corresponds to one of the two peaks seen in the 2 cm image (E2 at south-west, see Table 6).

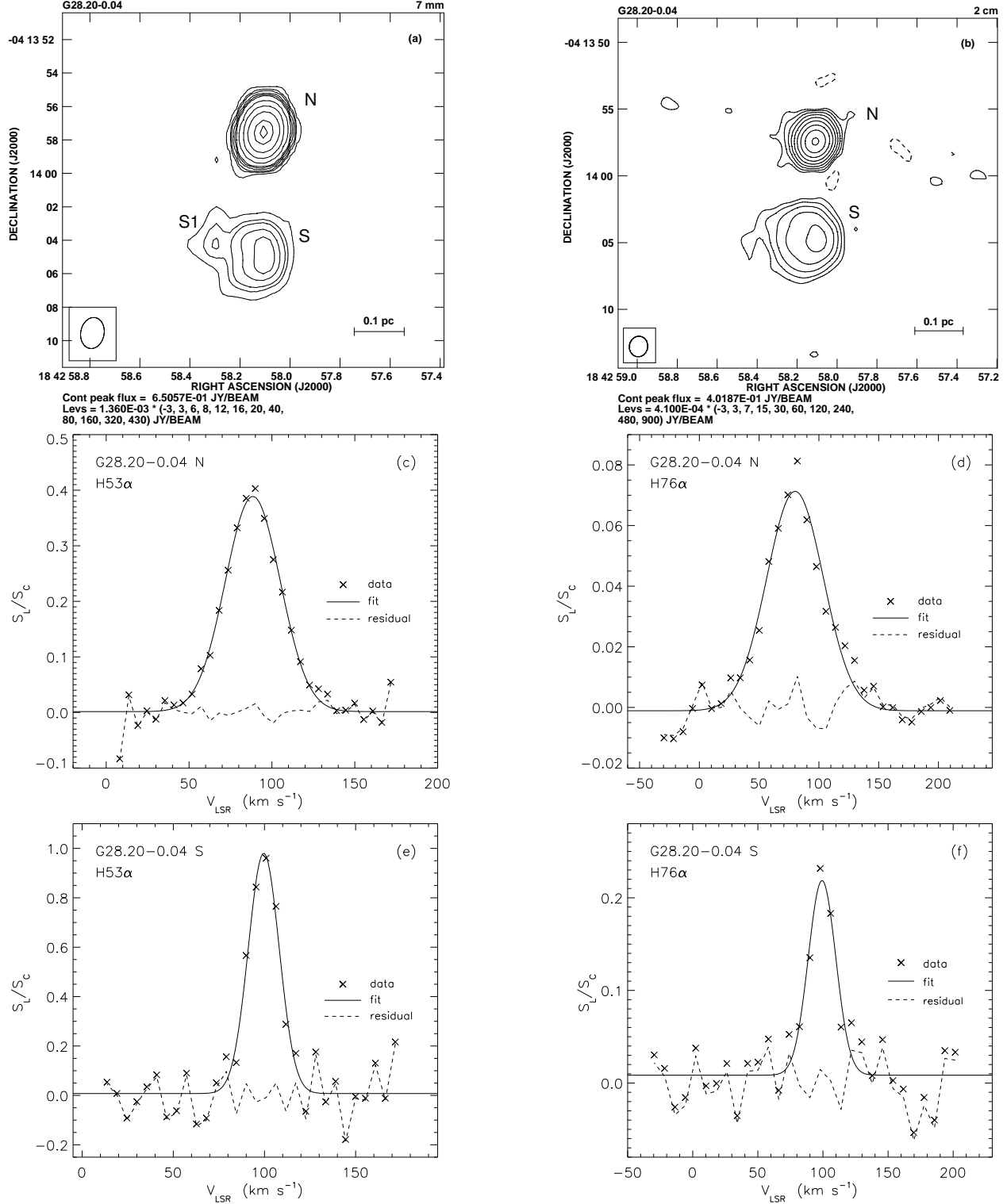


Fig. 3.— (a) The 7 mm VLA continuum image and the integrated H $53\alpha$  line profiles from the N (c) and S (e) components of MSFR G28.20. (b) The 2 cm VLA continuum image and the integrated H $76\alpha$  line profiles from G28.20 N (d) and S (f). The beam sizes shown in the lower left corners in (a) and (b) are  $\sim 1''.6$  and  $\sim 1''.4$ , respectively (see Table 1).

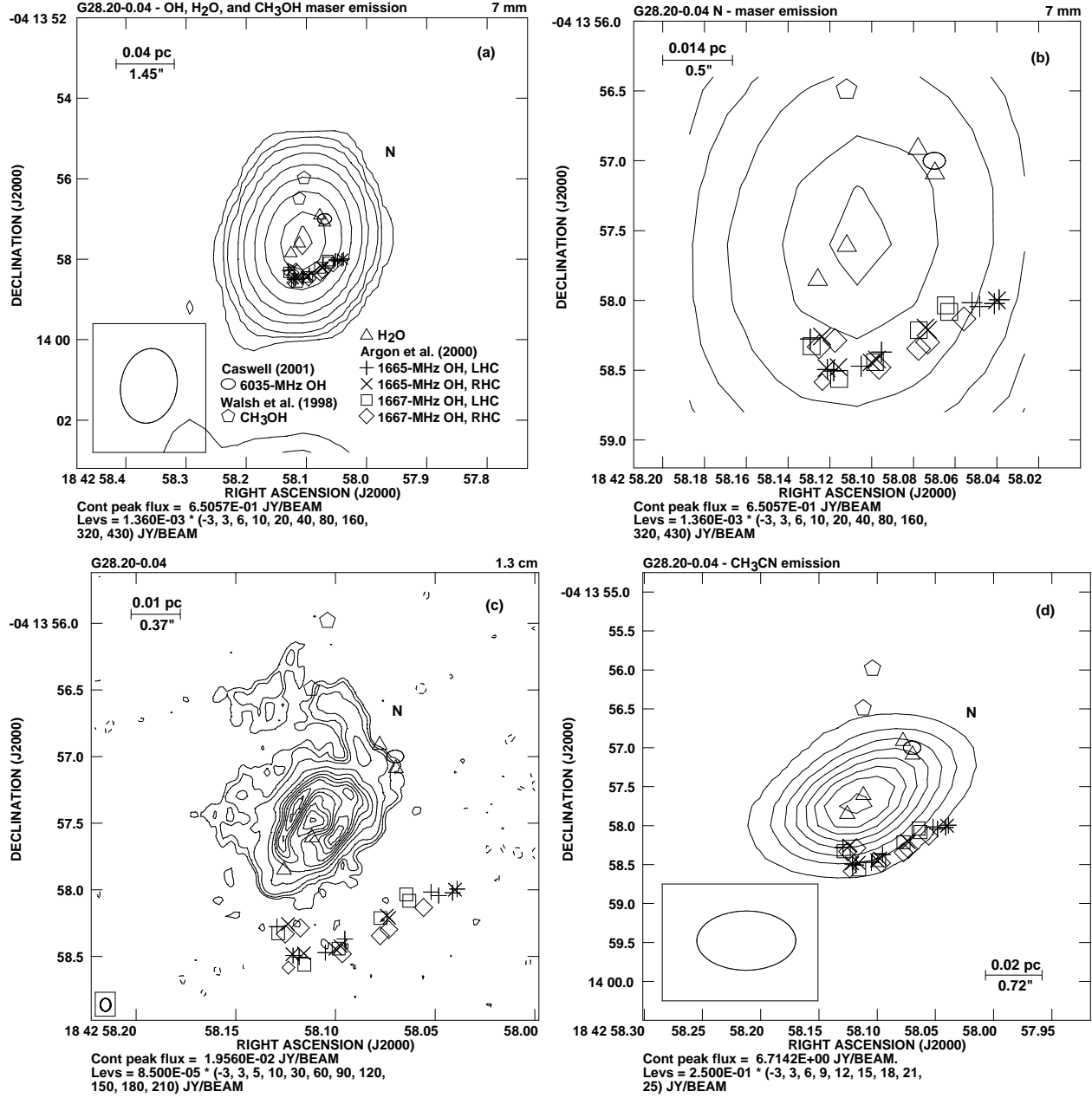


Fig. 4.— The distribution of OH and CH<sub>3</sub>OH masers in G28.20 N superimposed on: the 7 mm VLA image (a and b; b is a magnification of the central portion of the image shown in a; this paper), the 1.3 cm VLA image (c; VLA archival data, project AZ168), and the CH<sub>3</sub>CN SMA image (d; Qin et al. 2008). The synthesized beams of the VLA shown in the lower left insets in (a) and (c) are  $\sim 1''.6$  and  $0''.09$ , respectively (see Table 1). The synthesized beam of the SMA is  $\sim 1''.5$  (see Section 4.2) and is shown in the lower left corner in (d).

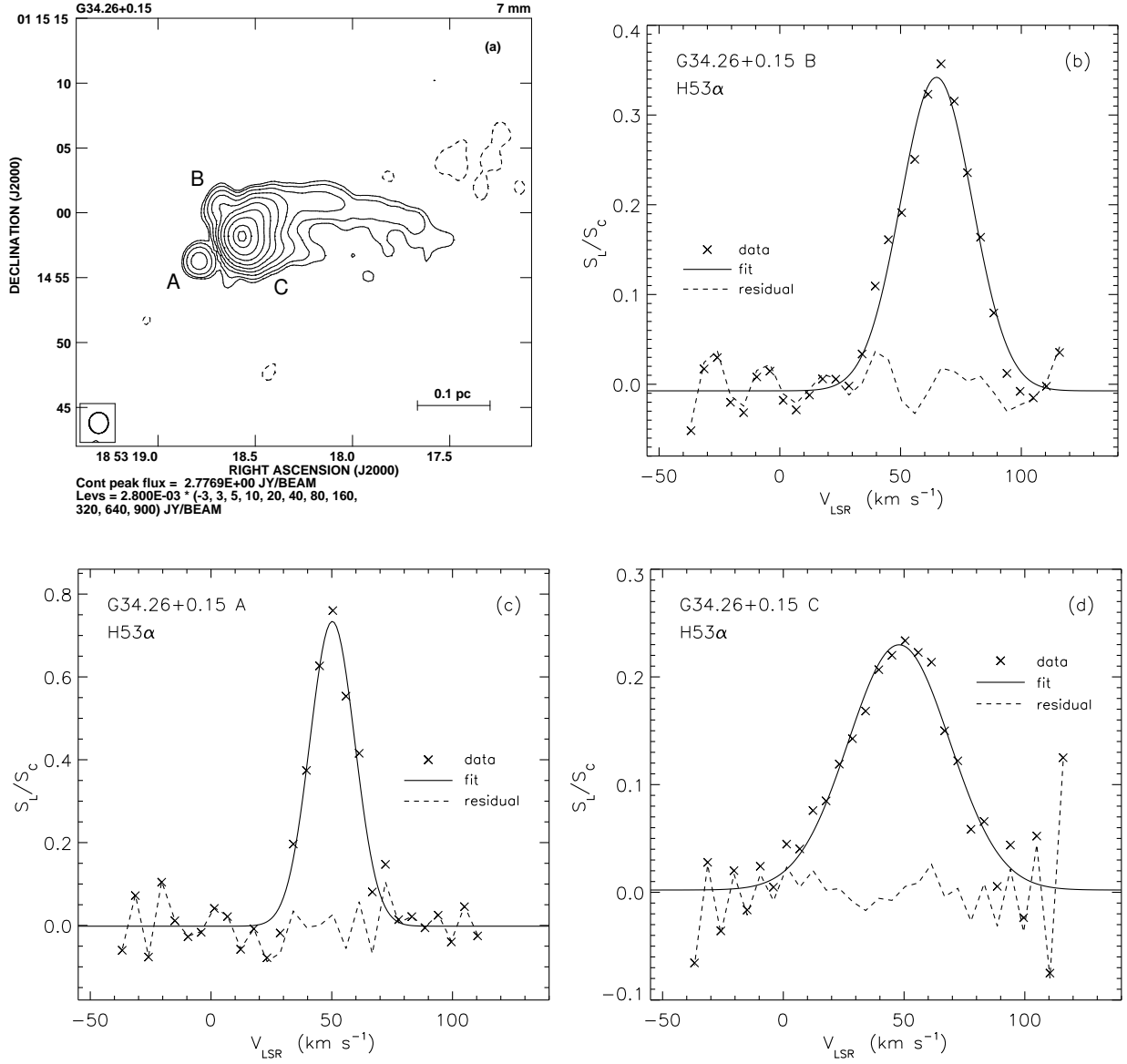


Fig. 5.— The 7 mm VLA continuum image (a) and the integrated H53 $\alpha$  line profiles from the A (c), B (b), and C (d) components of the MSFR G34.26. The beam size shown in the lower left corner in (a) is  $\sim 1.^{\circ}5$  (see Table 1).

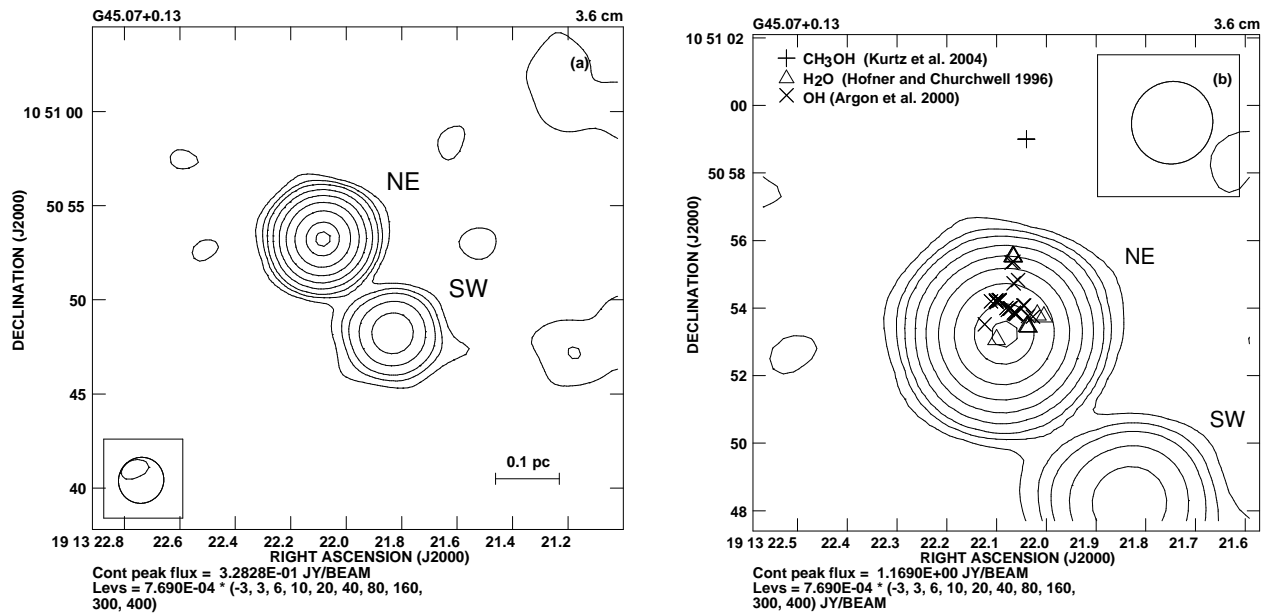


Fig. 6.— (a) The 3.6 cm VLA continuum image of the NE and SW components of the MSFR G45.07. (b) The magnification of (a) centered on G45.07 NE. Locations of 22 GHz H<sub>2</sub>O, 44 GHz CH<sub>3</sub>OH, 1665 MHz and 1667 MHz OH masers in the vicinity of G45.07 NE are indicated. The VLA beam is shown in both images (HPBW $\sim$ 2.<sup>5</sup>, see Table 1).

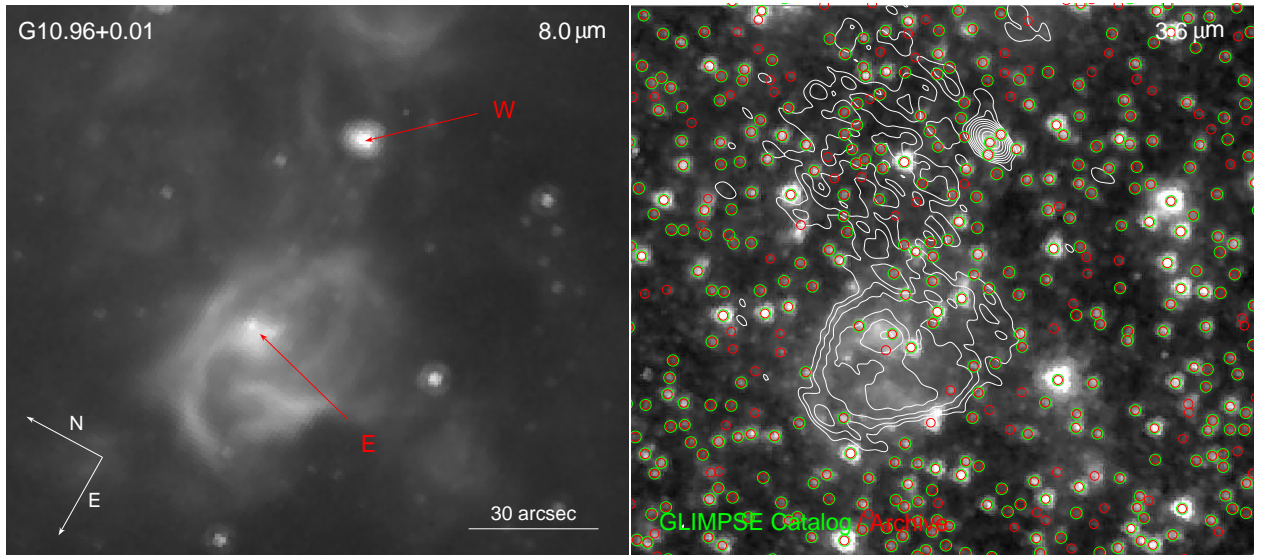


Fig. 7.— The IRAC 8.0 (*left*) and 3.6  $\mu\text{m}$  (*right*) images of G10.96. The positions of radio sources are indicated with red arrows in the 8.0  $\mu\text{m}$  image, while the 3.6 cm radio contours are overlaid on the IRAC 3.6  $\mu\text{m}$  image. The images are centered on the same coordinates and have the same size. The sources from the GLIMPSE Catalog and Archive are marked in the 3.6  $\mu\text{m}$  image with green and red circles, respectively. The intensity ranges from 0.5 mJy to 29.2 mJy for the 8  $\mu\text{m}$  image, and from  $\sim 1 \mu\text{Jy}$  to 22.4 mJy for the 3.6  $\mu\text{m}$  image. Thirty arcsec are equal to  $\sim 2$  pc assuming a distance of 14 kpc (see Table 2).

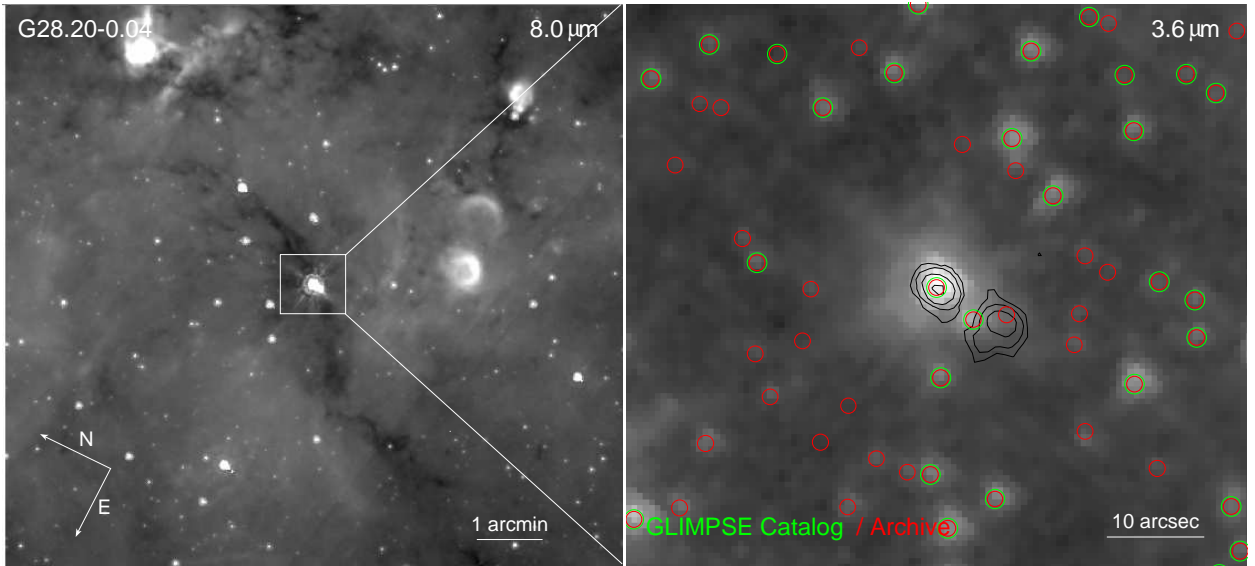


Fig. 8.— The IRAC 8.0  $\mu\text{m}$  (*left*) and 3.6  $\mu\text{m}$  (*right*) images of G28.20. The 8.0  $\mu\text{m}$  image shows that G28.20 is located toward an infrared dark cloud (see text). The 3.6  $\mu\text{m}$  image is zoomed in on the source; 7 mm radio contours indicate the positions of radio sources (see Figure 3a). The point sources from GLIMPSE are marked. The source appearing to be blended with G28.20 N slightly to the south in the 8  $\mu\text{m}$  image is an image artifact produced by the “electronic bandwidth effect” (see Section 2.2). The intensity ranges from 0.5 mJy to 51.2 mJy for the 8  $\mu\text{m}$  image, and from  $\sim 7 \mu\text{Jy}$  to 25.4 mJy for the 3.6  $\mu\text{m}$  image. One arcmin and 10 arcsec are equal to  $\sim 1.7$  pc and  $\sim 0.3$  pc, respectively, assuming a distance of 5.7 kpc (Table 2).

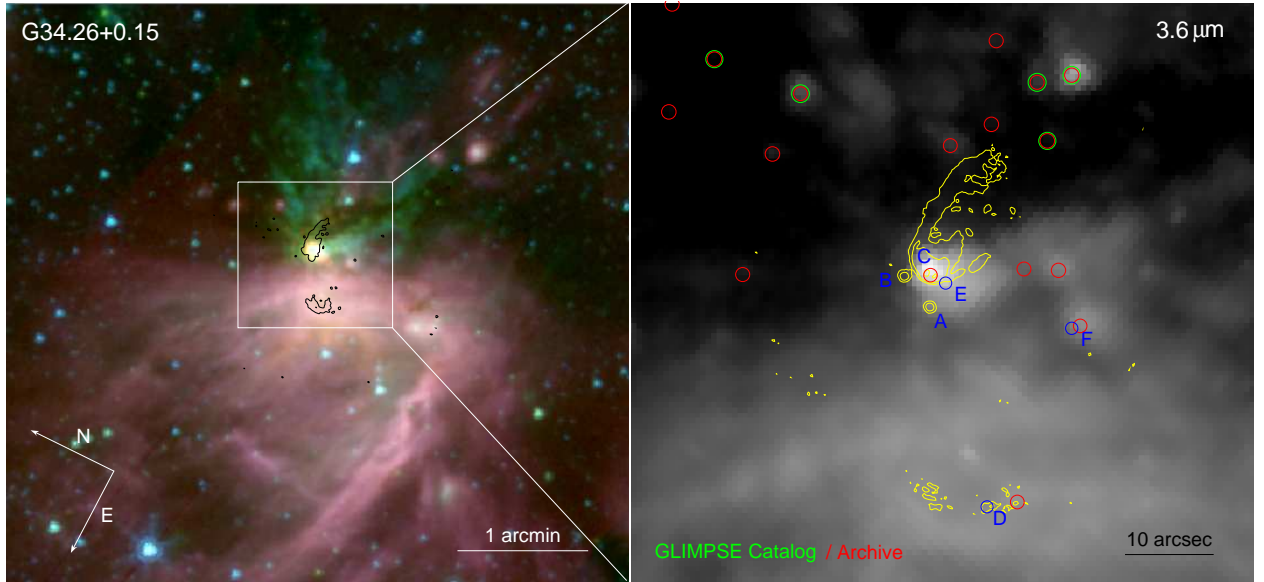


Fig. 9.— *Left:* The three color composite image of G34.26. Red, green, and blue correspond to IRAC 8.0  $\mu\text{m}$ , 4.5  $\mu\text{m}$ , and 3.6  $\mu\text{m}$ , respectively. The 7 mm  $3\sigma$  radio contour (see Figure 5) is overlaid to indicate the radio positions. A striking feature of the image is a massive outflow detected at 4.5  $\mu\text{m}$  (see Section 4.3.2). An incomplete ring of emission dominating the central and lower parts of the image corresponds to radio component D. *Right:* The IRAC 3.6  $\mu\text{m}$  image of G34.26 with the high-resolution 2 cm radio contours (Sewi $\ddot{\text{o}}$  et al. 2004a) overlaid. Mid-IR components E and F from Campbell et al. (2000) and the peak of radio D component (Fey et al. 1994) are marked with blue circles and labeled. The GLIMPSE point sources are marked. The 8.0  $\mu\text{m}$  image suffers from the “electronic bandwidth effect” (see Section 2.2). The intensity ranges are: ( $\sim 1 \mu\text{Jy}$ , 20.7 mJy), ( $\sim 1 \mu\text{Jy}$ , 23.4 mJy), and (0.3 mJy, 55.9 mJy) for 3.6, 4.5, and 8.0  $\mu\text{m}$  image, respectively. One arcmin and 10 arcsec are equal to  $\sim 1.1$  pc and  $\sim 0.2$  pc, respectively, assuming a distance of 3.7 kpc (see Table 2).

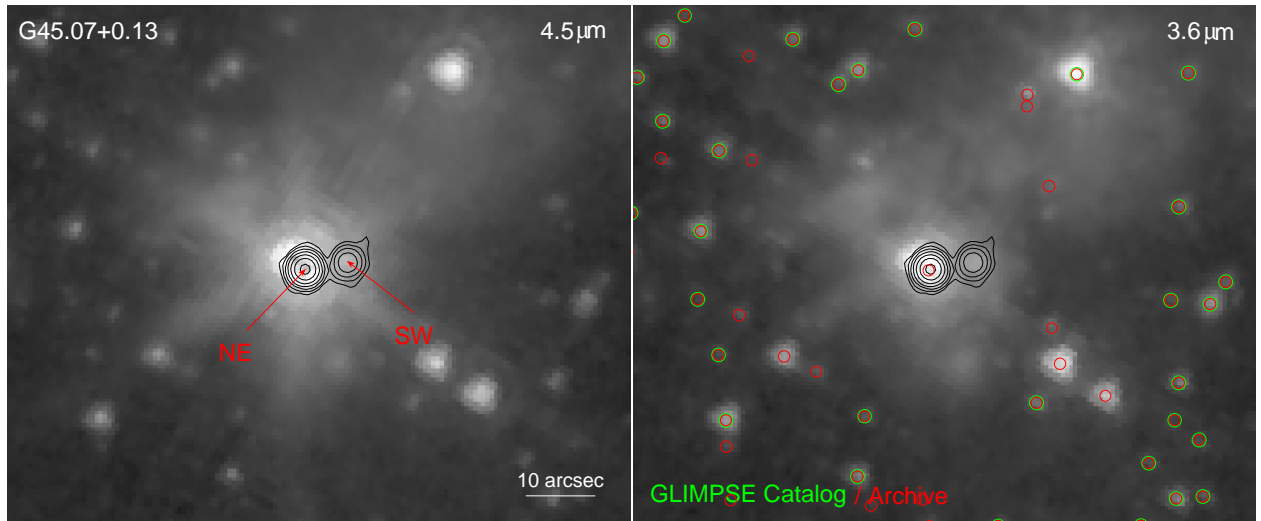


Fig. 10.— The IRAC  $4.5 \mu\text{m}$  (*left*) and  $3.6 \mu\text{m}$  (*right*) images of G45.07. The images have the same size. The  $3.6 \text{ cm}$  radio contours are overlaid on both images and the NE/SW components are indicated with red arrows in the  $4.5 \mu\text{m}$  image. Sources from the GLIMPSE Catalog and Archive are marked in the  $3.6 \mu\text{m}$  image with green and red circles, respectively. The intensity ranges from  $\sim 1 \mu\text{Jy}$  to  $28.8 \text{ mJy}$  for the  $4.5 \mu\text{m}$  image, and from  $\sim 1 \mu\text{Jy}$  to  $21.6 \text{ mJy}$  for the  $3.6 \mu\text{m}$  image. Ten arcsec are equal to  $0.3 \text{ pc}$  at a distance of  $6 \text{ kpc}$  (see Table 2).

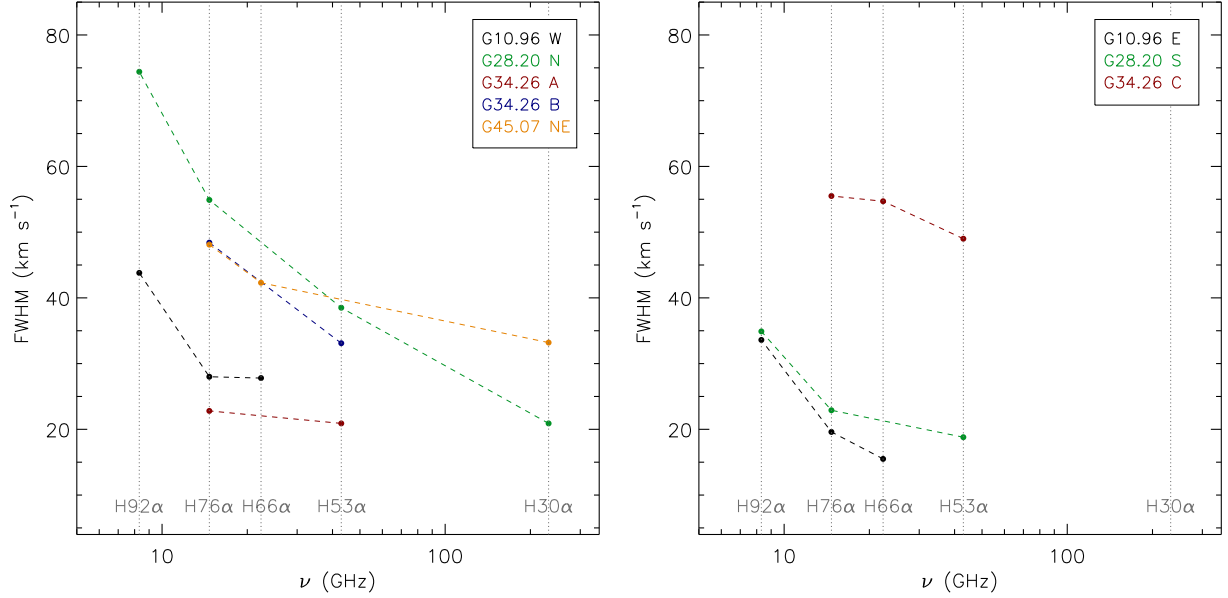


Fig. 11.— Plots showing the relation between the half-power widths of the RRLs (FWHMs) and frequency for HC H II region candidates (*left*) and UC H II regions (*right*) from our sample (Paper I and this paper). The plots include only the sources observed in more than one RRL. The FWHMs with the uncertainties, as well as references can be found in Section 4. The values measured in this paper are also listed in Table 8. See the discussion of the plot in text (Section 5.1).

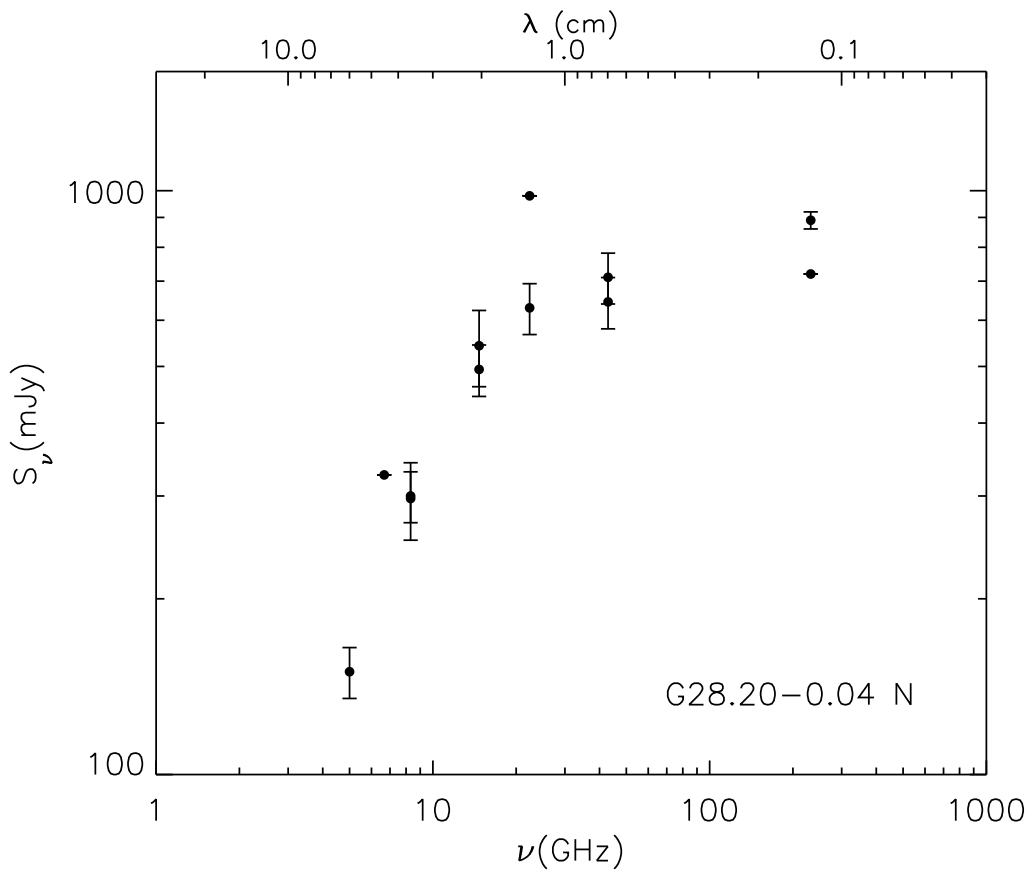


Fig. 12.— Spectral energy distribution of G28.20 N from 5 GHz to 231.9 GHz. Flux densities and beam sizes, along with references, are listed in Table 9. The uncertainties are plotted when available.